

10-10-2018

The Sedimentology and Origins of a Giant Mass Transport Complex: The Nataraja Slide, Arabian Sea

Sarah Dailey

Louisiana State University and Agricultural and Mechanical College

Follow this and additional works at: https://repository.lsu.edu/gradschool_theses



Part of the [Geochemistry Commons](#), [Geology Commons](#), and the [Sedimentology Commons](#)

Recommended Citation

Dailey, Sarah, "The Sedimentology and Origins of a Giant Mass Transport Complex: The Nataraja Slide, Arabian Sea" (2018). *LSU Master's Theses*. 4802.

https://repository.lsu.edu/gradschool_theses/4802

This Thesis is brought to you for free and open access by the Graduate School at LSU Scholarly Repository. It has been accepted for inclusion in LSU Master's Theses by an authorized graduate school editor of LSU Scholarly Repository. For more information, please contact gradetd@lsu.edu.

THE SEDIMENTOLOGY AND ORIGINS OF A GIANT MASS
TRANSPORT COMPLEX: THE NATARAJA SLIDE, ARABIAN SEA

A Thesis

Submitted to the Graduate Faculty of the
Louisiana State University and
Agricultural and Mechanical College
in partial fulfillment of the
requirements for the degree of
Master of Science

in

The Department of Geology and Geophysics

by
Sarah Dailey
B.A., University of Houston, 2015
December 2018

ACKNOWLEDGMENTS

I would first like to express my appreciation to Dr. Peter D. Clift for his patience and guidance in writing this thesis. His positive attitude, friendliness, and generosity to me during the past two years has been exceptional. I would also like to thank my committee members, Dr. Carol Wilson, and Dr. Guangsheng Zhuang, for their advice and help with drafts.

Thank you to the Department of Geology and Geophysics at Louisiana State University and especially the head of the department, Dr. Carol Wicks. Her advice and guidance in the classroom, and out, is very appreciated.

Thank you to my family and all of my friends. Especially thank you to my mom and dad. Without their support and encouragement, I wouldn't have gotten through the last two years.

TABLE OF CONTENTS

| | |
|---|----|
| ACKNOWLEDGMENTS..... | ii |
| ABSTRACT | iv |
| 1. INTRODUCTION | 1 |
| 1.1 IODP Expedition 355..... | 1 |
| 1.2 Geology of Mass Transport Complexes | 2 |
| 1.3 Previous Studied Mass Transport Complexes | 4 |
| 1.4 Study Area..... | 6 |
| 1.5 Geologic Setting and Background | 9 |
| 2. OBJECTIVES | 12 |
| 3. METHODS | 13 |
| 4. RESULTS | 17 |
| 4.1 Top and Bottom | 17 |
| 4.2 Lithologic Logs | 21 |
| 4.3 Sedimentary Facies | 23 |
| 4.4 Microscopic Facies | 33 |
| 4.5 Geochemistry | 35 |
| 5. DISCUSSION..... | 43 |
| 5.1 Depositional Mechanisms | 43 |
| 5.2 Triggering Mechanisms | 44 |
| 5.3 Other Mass Movements | 46 |
| 6. CONCLUSIONS | 48 |
| BIBLIOGRAPHY..... | 50 |
| APPENDIX | 56 |
| Table 1: Bulk Geochemistry | |
| Table 2: Neodymium and Strontium Isotopes | |
| Table 3: Clay Mineralogy | |
| VITA | 60 |

ABSTRACT

A giant mass transport complex (MTC) was recently discovered in the eastern Arabian Sea exceeding in volume all but one other known complex on passive margins worldwide. The complex, named the Nataraja Slide, was drilled by IODP Expedition 355 in two locations where it is ~300 m (Site U1456) and ~200 m thick (Site U1457). The top is defined by the presence of both reworked microfossil assemblages and deformation structures, such as folding and faulting. The deposit consists of two main phases of mass wasting, each which consists of smaller pulses, with generally fining upward cycles, all emplaced just prior to 10.8 Ma. The base of the deposit at each site is composed largely of matrix-supported carbonate breccia that is interpreted as the product of debris flows. In the first phase, these breccias alternate with very well-sorted calcarenites deposited from a high energy current, coherent limestone blocks that are derived directly from the Indian continental margin, and few clastic mudstone beds. At the top of the deposit, in the second phase, muddy turbidite deposits dominate and are increasingly more siliciclastic in composition. At Site U1456, where both phases are seen, a 20 m section of hemipelagic mudstone is present, that is overlain by a ~40 m section of calcarenite and slumped interbedded mud and siltstone. Bulk sedimentary geochemistry, clay mineralogy, and isotope analysis constrain the provenance of the clastic, muddy material to reworked Indus-derived material, with some input from smaller western Indian rivers (e.g., Narmada and Tapti Rivers), and some material from the Deccan Traps. The carbonate material is a shallow-water limestone from the outer western Indian continental shelf that was likely oversteepened from enhanced clastic sediment delivery during the mid-Miocene. The final emplacement of the material was likely related to seismicity as

there is evidence for intraplate earthquakes immediately opposite of the scar. Although I hypothesis this area is at low risk of future mass wasting events, it should be noted that other continental margins around the world could be at risk for mass failure as large as the Nataraja Slide.

1. INTRODUCTION

1.1 IODP Expedition 355

In spring 2015, International Ocean Discovery Program (IODP) Expedition 355 drilled at Sites, U1456 and U1457 in the eastern Arabian Sea, which recovered sediment from a mass transport complex (MTC), known as the Nataraja Slide. The main objective of the expedition was to sample the turbidite sequences of the Indus Submarine Fan and the underlying basement in order to reconstruct and understand the long-term development of the regional tectonics, climate, and erosional history of the Arabian Sea region (Pandey et al., 2015). Preliminary descriptions were collected by the scientists of Expedition IODP 355. Here I interpret the section of core that includes the giant MTC, the Nataraja Slide.

The Nataraja Slide is essential to study because it's the second largest known submarine landslide on a passive margin with the unique accessibility to over 500 meters of core. The deposit allows the interpretation of the internal character and architecture of a giant MTC with a large run-out distance and multiple phases. I use traditional sedimentary geological methods to define facies and depositional processes, coupled with geochemical and petrographic data to constrain provenance in addition to what has been defined from seismic data.

1.2 Geology of Mass Transport Complexes

MTC's have a fundamental role in shaping the morphology along coastlines, continental slopes, and deep-water basins (Elverhoi et al., 2010). These mass movements play a dominant role in the mobilization and deposition of sediment from shallow shelves to the deep sea (Nardin et al., 1979). They can be characterized by their large size, distinctive morphology, and chaotic internal character (Shipp et al., 2011). Many MTCs

show similar features and morphologies including a scarp, head, body of displaced material, and the toe (Hampton and Locat, 1996; Masson et al., 2010). The term mass transport includes the failure, dislodgment, and downslope movement of sediment under the influence of gravity (Shanmugam, 2011). The initiation of these deposits can be difficult to understand and can be attributed to a number of processes. Sediments can be pre-conditioned to failure at the time of their deposition because of increased sediment delivery rates, glacial history, and tectonic uplift (Masson et al., 2010). Mass movements can also occur from triggering events such as earthquakes (Bryn et al., 2005), gas hydrate destabilization (Mienert et al., 2005), and deep ocean currents (Embley, 1952). Some areas are prone to repeated mass movements where the cause of sliding, such as increase of sediment delivery rates on a submarine or subaqueous delta, persists over long periods of time (Masson et al., 2006). Glacial/interglacial transitions are other conditions that can contribute to repeated mass movements (Bryn et al., 2005) and post-glacial isostatic rebound could serve as the final triggering event to cause the movement (Evans et al., 2012). Areas considered landslide prone are fjords, river deltas, submarine canyon-fan systems, continental slope, and ocean volcanic islands (Hampton et al., 1996). The slope failure can occur over a range of slopes from $\sim 0.5^\circ$ in the Mississippi delta (Walker and Massingill, 1970) to $\sim 1^\circ$ in the Storegga area (Bryn et al., 2005), to almost 10° along ocean island flanks (Sawyer et al., 2009). These mass movements undergo significant change as they travel from the source to the basin floor (Covault, 2011). This movement can involve a number of processes including creep, sliding, rock falls, slumping, debris flow, turbidity currents, and debris avalanches (Normark et al., 1993, Middleton and Hampton, 1973). The force of gravity, among other factors, plays an essential role in the

mechanics of these processes (Hampton et al., 1996) and the proportion of sediment and fluid in the flow controls the type of process.

Previous literature defines the terms associated with MTCs in many different ways. It should be noted that the nomenclature is complex and there is an overlap in the use of many terms. Slides can be separated from slumps, and other downslope movements, and defined as a coherent mass with translational movement and continuous bedding (Dott, 1963; Nardin et al., 1979). Slumps are defined as a coherent mass with rotational movement and internal deformation. Further deformed, debris flows are laminar, cohesive flows which are supported by their matrix strength and exhibit plastic mechanical behavior (Masson et al., 2006, Nardin et al., 1979). Debrites can show sharp upper contacts, inverse grading, and can include a variable clast size and rafts. Following the classification of Middleton and Hampton (1973), I will include turbidity currents as a type of mass movement or mass flow. As the fluid content increases, a plastic debris flow will turn into a turbidity current, which is supported by fluid turbulence (Nardin et al., 1979). Turbidity currents have a viscous fluid behavior and have low sediment concentrations (Nardin et al., 1979; Shanmugam, 2011). The different processes occurring as the sediment mass moves downslope largely depends on the sediment grain size and sediment concentration (Nardin et al., 1979). The mechanical behavior of sediments as they move downslope range from elastic to plastic to viscous and can sometimes be a combination of these (Dott, 1963). The transition between the processes involves a change in the physical state of the sediment (Nardin et al., 1979). There is a continuous translation between slides, slumps, and gravity flows, and many MTCs show

a mixture of all three. Defining the balance between these for the very largest MTCs is a primary goal of my research.

1.3 Previous Studied Mass Transport Complexes

Areas of importance to the petroleum industry or areas at great risk to tsunami hazards are intensely studied by scientists. The Agulhas Slump, found along the coast of South Africa, is 20,331 km³ in volume, making it the only known larger deposit than the Nataraja Slide (Dingle, 1977). One of the most intensely studied submarine landslides, the Storegga Slide, off the coast of Norway, comprises a volume of ~5,000 km³ from three separate events (Bugge et al., 1988; Bryn et al., 2005). Slumping on the Mississippi River Delta is also highly studied because of its proximity to offshore petroleum structures (Prior and Coleman, 1978; Walker and Missingill, 1970). Studies of MTCs have recently been done using 3D seismic reflection profiles because of the inability of workers to access sites of submarine landslides and insufficient funds to collect many or deep-penetrating cores. This sets limits to the conclusions of these studies because of assumptions used without direct evidence from the deposits. The features seen in reflection profiles can be deceiving without appropriate ground truthing. Large blocks in a reflection profile may be interpreted as allochthonous, thereby associated with a submarine landslide, which in reality are only in-place topographic highs (Hampton and Locat, 1996). This is because deep-penetrating seismic waves can be limited in their resolution as a result of the wavelength being relatively large compared to many geological features. Other studies have been done to simulate the movement of material downslope using numerical modeling (Elverhoi et al., 2010; Masson et al., 2006, De Blasio et al., 2005). However, a disadvantage to this approach is the size constraint.

Laboratory simulations can only model small landslides, and as shown in the deposit I describe here, MTCs can reach thousands of cubic kilometers in size. Much previous work has also incorporated the physical properties of drill core such as shear strength, compressional velocity, resistivity, density, and porosity (Weimer and Shipp, 2004). An increase in the resistivity can be correlated to an increase in bulk density and shear strength, which relates to the presence of an MTC. This, however, can only be accurately collected to a certain depth. Ideally, a scientist will have access to core, seismic, and log data for a complete understanding of the internal architecture of the deposit.

Understanding how MTCs affect the bathymetry of sedimentary basins and the natural hazards that result from them is important in natural hazard prediction and mitigation, and should be continually researched.

1.4 Study Area

The Nataraja Slide is located off the western margin of India, in the Eastern Arabian Sea (Fig. 1). It lies within the Laxmi Basin which is bordered by the Laxmi Ridge to the west and the Indian continental shelf to the east. The slide runs from the Gujarat-Saurashtra margin to the Laxmi Basin (Calves et al., 2015). The Panikkar Seamount, Raman Seamount, and Wadia Guyot, collectively referred to as Panikkar

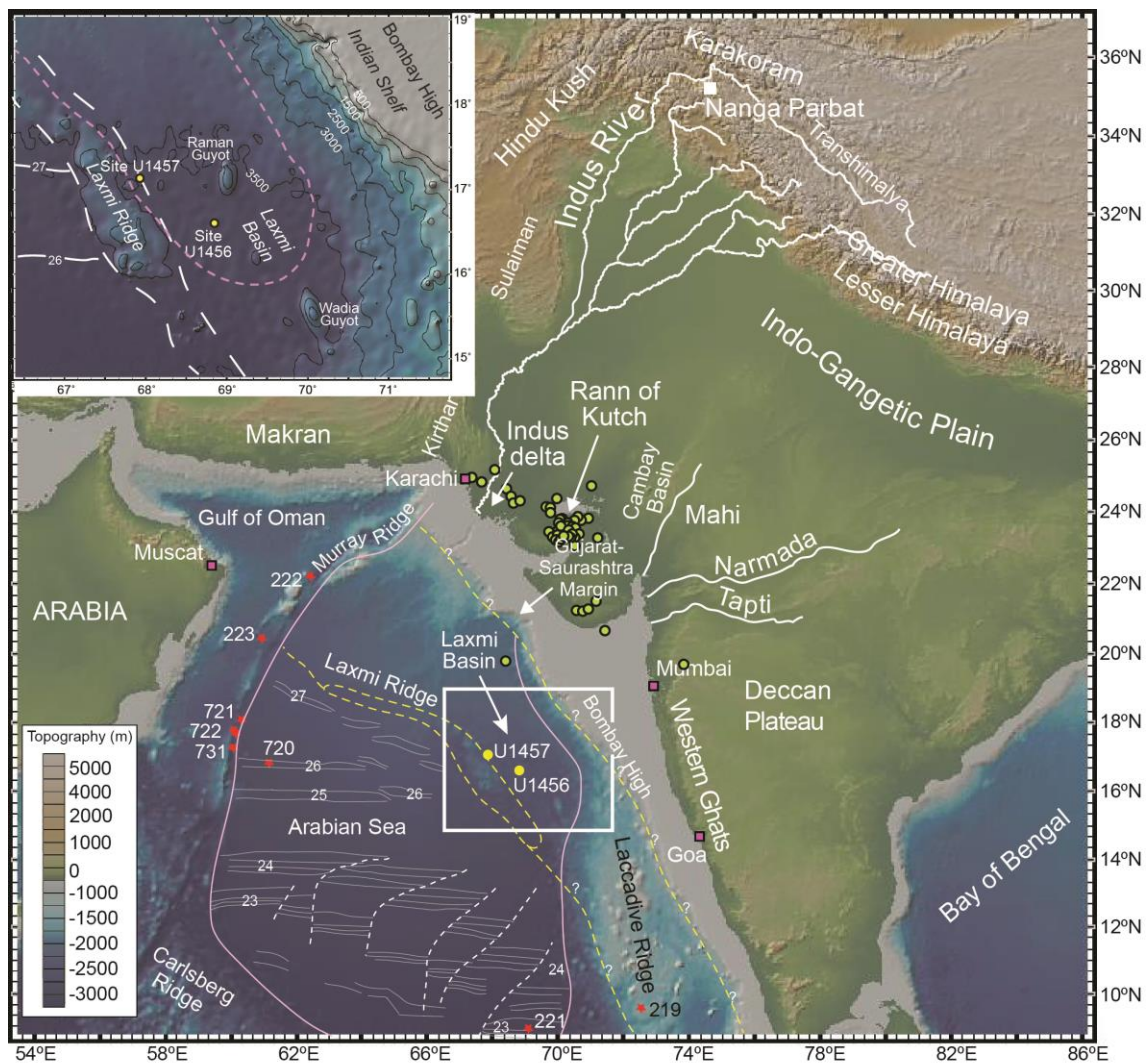


Figure 1. Shaded bathymetric map of the Arabian Sea showing the location of the core sites (yellow circles) discussed in this study. Pink dashed line shows an estimate of where the Nataraja Slide lies. Modified from Pandey et al., 2016. Base map from GeoMapApp.

Ridge, are present along the axial part of the Laxmi Basin. (Pandey et al., 2016). Site U1456 lies ~475 km from the Indian Coast and ~820 km from the mouth of the Indus River. Site U1457 lies ~490 km from the Indian Coast and ~750 km to the south of the mouth of the Indus River (Pandey et al., 2016). The MTC covers a length of over 330 km and is a maximum of 190 km wide (Calves et al., 2015). The headwall was predicted to be located in the slope of the Gujarat-Saurashtra Basin. It contains slope-gradients ranging from 1.6° to 2.7° and the distal lower half of the mass transport deposit lies at a gradient of 1.2° (Calves et al., 2015).

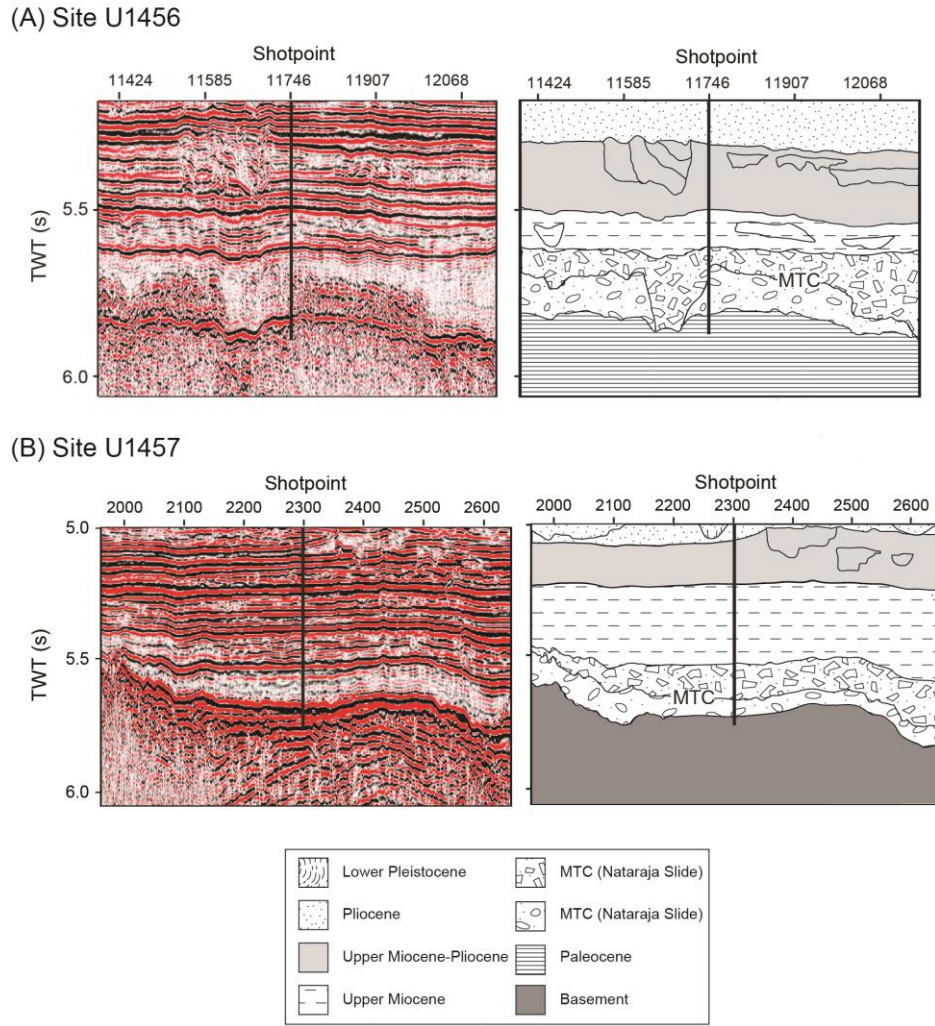


Figure 2. Seismic line of the core sites with interpretation showing the MTC at (A) IODP Site U1456 and (B) IODP Site U1457. Modified from Pandey et al., 2016

Calves et al. (2015) named and defined the Nataraja Slide from interpretation of two-dimensional seismic reflection profiles. It was defined by the chaotic nature of the reflectors. The continuous reflectors show the deposit is one large body. However, in detail, close to Site U1456 (Fig. 2A) there are recognizable heterogeneities in the seismic reflections that can be correlated to the drill core, and imply emplacement in more than one phase, and with more than one depositional mechanism. The section of the MTC

drilled at Site U1457 is considerably thinner than at Site U1456, and can be explained by the location being on the distal end of the complex (Fig 2B). They recognized this as the second largest MTC known on a passive margin, representing a volume of $\sim 19,000 \text{ km}^3$.

1.5 Geologic Setting and Background

The western margin of India is a rifted passive continental margin and is characterized by a very wide shelf (Pandey and Pandey, 2015). It is associated with the break-up of India and the opening of the Arabian Sea (Pandey and Pandey, 2015). The Arabian Sea basin formed as a result of seafloor spreading between India and Madagascar in the mid-Cretaceous, and Seychelles during late-Cretaceous (Norton, 1979). The final phase of rifting is associated with Deccan volcanism (Pandey et al., 2015). Eruption of continental flood basalt, from the Reunion hotspot, occurred on the western mass of India and subsequently emplaced magmatic intrusions within the crust (Devey and Stephens, 1991). This is the main event to have shaped onshore India (Mahoney, 1988).

The continental shelf consists of rollover anticlines and several faults in parallel sets that came into existence in the late Cretaceous (Biswas, 1982). These normal faults bound horsts that correspond to crust deformation during the rifting process (Nair and Pandey, 2018). Several seismic ridges and adjoining basins are present along the western margin of India. The Laxmi Ridge, a rifted Indian continental sliver, running parallel to the Indian continental margin, separates the Arabian Sea into two basins. The eastern basin lies between the continental margin and the Laxmi Ridge, and the western basin lies between the Laxmi Ridge and the Carlsberg Ridge, where present active spreading is occurring (Krishna et al., 2006).

The eastern Arabian Sea consists of several subbasins. One of which is the Laxmi Basin, where the Nataraja Slide lies. Within the Laxmi Basin are an array of seamounts, the Raman, Panikkar, and Wadia Guyot, collectively referred to as the Panikkar Ridge (Krishna, 2006). These are volcanic in nature, formed during the Deccan volcanism. The nature of the crust beneath the Laxmi Basin is controversial in literature, but is generally interpreted as stretched continental crust (Krishna, et al., 2006, Clift et al., 2002). Post rifting in the Arabian Sea, around 50 Ma, India's northward drift resulted in continent–continent collision that gave rise to the Himalayan Orogeny (Clift et al., 2002; Nair and Pandey, 2018, and references therein). This caused development of fan systems like the Indus Fan, the main sedimentary body in the Arabian Sea, and an increase of sediment supply to the Indian margin, that could be a preconditioning factor to the mass wasting presented here. Indus sediments cover much of the Panikkar Ridge, which is only elevated above the seafloor by the seamounts (Krishna et al., 2006). Along with the higher clastic supply, oil exploration has also identified multiple carbonate build ups within the continental shelf, specifically during the Miocene.

North of the Laxmi Basin is the Gujarat- Saurashtra basin and Saurashtra platform where the headwall of the Nataraja Slide is located. The margin offshore the Saurashtra platform is composed of a deep-water fold and thrust belt that, along with the increase of clastics, could have caused slope steepening (Calves et al., 2015). The Bombay High, a large paleohigh, is situated off the coast of India, south of the Saurashtra platform. It was formed by a fault on its eastern flank, and within the Deccan Traps to the east, has a downthrow of ~800-1000 meters (Sahay, 1979).

The area has been largely seismically inactive except towards the north where the Rann of Kutch forms an active structure within the Indian Craton, and which has been linked to flexure of the plate as a result of the collision between India and Asia (Bilham et al., 2003; Biswas, 2005). This is presumed to have started in the Eocene (Najman et al., 2010) or even earlier (DeCelles et al., 2014). Towards the north, the Indian peninsula is cut by the NE-SW trending Cambay Basin which formed as an initial early Cretaceous rift that was then reactivated in the Cenozoic and experienced significant inversion in the early Miocene (Chowdhary, 2004).

2. OBJECTIVES

The purpose of this research is to:

- Describe the internal architecture and characteristics of the Nataraja Slide mass transport complex (MTC). Combining the descriptions of the core with the facies interpretations, and inferred depositional mechanisms will give me a fuller understanding of the structure and spatial organization of the MTC and allow future scientists to better understand other giant submarine landslides that are less well imaged and sampled.
- Explain the depositional mechanisms that allowed the emplacement of the deposit. By defining the different processes that occurred based on the observed facies, I will reconstruct the history of the movement from slope to deep sea.
- Determine the provenance of the sediment. I will constrain where the clastic and carbonate material came from, which in turn has implications for the triggering and emplacement processes.
- Constrain the original triggering mechanism. This is important if geologists are going to be able to recognize similar issues in other areas of the world for future hazard warning and mitigation.
- Create a conceptual model of the multistage process that occurred from initial failure to final emplacement.

3. METHODS

Although the sedimentary cores collected during Expedition 355 were described during the cruise, I re-examined several of these as part of this study in order to obtain more detailed descriptions of critical sedimentary structures based on the initial shipboard interpretations to guide more detailed work. I examined the core for bedding contacts, bed thickness variations, grain-size variations, composition, primary physical sedimentary structures, biogenic sedimentary structures, and post-depositional sedimentary structures. In addition to preparing detailed sedimentary logs designed to highlight the different sedimentary facies, I also sampled the sediment for microscope thin section descriptions in order to provide an overview of the different sediment types both at macro and microscopic scales. Forty polished thin sections were made of clastic and carbonate rock samples by Quality Thin Sections in Tuscan, Arizona. These were viewed under a petrographic microscope at Louisiana State University to constrain the mineralogy of the deposit. Fossils and microfacies analysis can be used to constrain the initial depositional setting and so further allow the origin of the MTC to be understood. Microfossils identified in the deposit can be used to constrain the age of the sediments and potentially the depth of the original detachment within the continental margin stratigraphy.

Geochemical methods were employed to constrain the provenance of the materials and in particular to verify the Western Indian continental margin source for much of the MTC. Very little siliciclastic coarse-grained sediment was identified restricting our methods to bulk geochemistry, neodymium (Nd) and strontium (Sr) isotope analysis and semiquantitative clay mineralogy of decarbonated sediment.

The major element compositions together with select trace elements (Ba, Zr, Sr) of forty-four decarbonated samples were determined by Inductively Coupled Plasma Emission Spectrometry (ICP-ES) at Boston University, with precision quantified to be better than 2% of the measured value for all elements. Accuracy was constrained by analysis of certified Standard Reference Materials (BHVO-2), and results were accurate within precision. Table 1 provides the results of the repeated analyses of the standard, as well as the analyses of the samples.

The Nd isotopic compositions of sediments are generally considered to be minimally affected by chemical weathering such that source terranes faithfully translate their isotopic signature to eroded sediments (i.e., (Goldstein et al., 1984)). Sr isotopes are additionally considered, while recognizing that compositions may be affected by chemical alteration (Derry and France-Lanord, 1996). Caution was taken to decarbonate samples prior to analysis because Sr isotopes are strongly affected by the presence of carbonate. Although we recognize the Sr isotopic budget is likely controlled in part by this carbonate fraction, this study targets siliciclastic sediment compositions only in accord with previous studies for the Indus River, fan and delta. Twenty-five samples, of which were also analyzed for bulk geochemistry, were selected throughout the deposit at Sites U1456 and U1457 for the determination of $^{143}\text{Nd}/^{144}\text{Nd}$ and $^{87}\text{Sr}/^{86}\text{Sr}$ values. The clastic samples were first decarbonated with 20% acetic acid. Decarbonation lasted for 5-6 days until no further fizzing was observed with new acid. Samples were washed by deionized water before being ground into powders. Nd and Sr isotopic compositions were determined by Finnigan Neptune multi-collector inductively coupled plasma mass spectrometer (MC-ICP-MS) at Woods Hole Oceanographic

Institution. Nd and Sr isotope analyses were corrected against La Jolla Nd standard $^{143}\text{Nd}/^{144}\text{Nd}=0.511847$ and NBS987 standard $^{87}\text{Sr}/^{86}\text{Sr}=0.710240$. Procedural blanks for analyses were 20–25 pg for Sr (and 50–70 pg for Nd). We calculate the parameter ϵ_{Nd} (DePaolo and Wasserburg, 1976) using a $^{143}\text{Nd}/^{144}\text{Nd}$ value of 0.512638 for the Chondritic Uniform Reservoir (CHUR (Hamilton et al., 1983). Results are presented in Table 2.

Clay mineralogy was examined mostly for provenance purposes since different environmental conditions and source terranes result in the generation of contrasting assemblages, allowing us to separate material derived from the Indus River from those more closely linked to peninsular India. Although there may have been some change in mineralogy during initial diagenesis, the relatively shallow burial depths of these cores means there is no significant thermal diagenesis. This suggests the observed mineralogy would be largely representative of that at the time of sedimentation.

Clay mineralogy was determined by using X-Ray Powder Diffraction (XRD) at Louisiana State University using a Panalytical Empyrean X-Ray Diffractometer. Forty selected samples within the MTC were decarbonated for 5 to 6 days and soaked in water until there was no flocculation, with Na_3PO_4 added to de-flocculate when necessary. Four XRD patterns were generated from each oriented sample smear. The first was collected from the sample in air-dried condition. The slide was then placed in a desiccator with ethylene glycol for a minimum of 8 h at 25°C, and the second XRD pattern was generated from a glycolated sample. The third and fourth XRD data sets were collected after the sample was subjected to heat treatments of 300°C for 1 h, and then 550°C for 1 h, respectively. XRD analysis began immediately after glycolation, and immediately after

the first heat treatment. In this study, we use the semi-quantitative method of Biscaye (1965) to estimate the clay assemblage, which is based on peak-intensity factors determined from calculated XRD patterns as measured by MACDIFF software. For clay minerals present in amounts >10 wt% uncertainty is estimated as better than ± 5 wt% at the 95% confidence level. Uncertainty of peak area measurement based on repeated measurements is typically <5%. Data are presented as relative concentrations of the total clay assemblage in Table 3.

Biostratigraphy of the deposit was conducted by Denise Kalhunek while onboard the IODP expedition 355 (Pandey et al., 2016). These results show where the sediment is reworked versus where hemipelagic sedimentation has occurred, and is used for constraining an age range of the sediment and depth on the continental shelf.

4. RESULTS

4.1 Top and Bottom

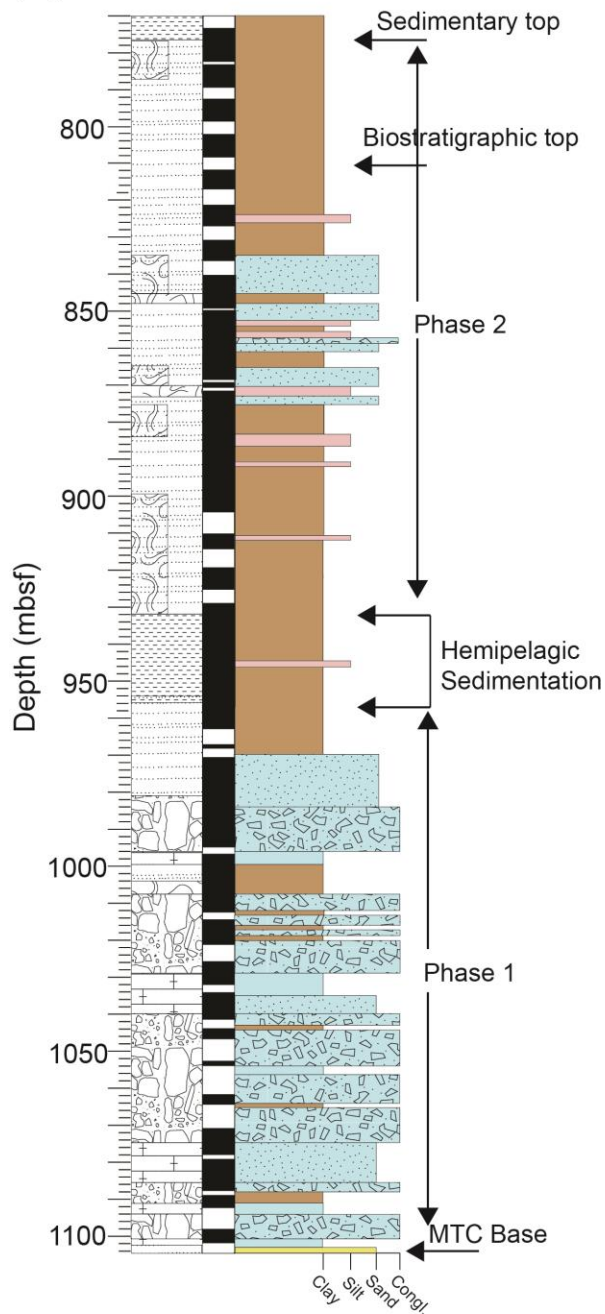
Microfossil assemblages within the sediments provide constraints on the age of emplacement. The oldest sediment overlying the MTC was dated at around 10.8 Ma based on nannofossil assemblages and paleomagnetic stratigraphy (Pandey et al., 2016c). In Hole U1456D the first appearance of *Discoaster hamatus* (10.55 Ma) marks the top of Zone NN8 (Pandey et al., 2016a), while in Hole U1457C the interval 859.49–995.93 meters below the seafloor (mbsf) contains *Catinaster coalitus*, which spans an age range of 9.69–10.89 Ma (Pandey et al., 2016b). The presence of *Discoaster bellus* (first appearance at 10.40 Ma) was also identified. In combination, these microfossil assemblages constrain the age for this interval within the MTC to between 9.69 and 10.40 Ma. Much of the interval from 1009.21 to 1054.34 mbsf at Site U1457 contains a mixture of different nannofossil species.

Above the MTC there is a coherent assemblage of nannofossils suggestive of hemipelagic sedimentation, and not the mixed assemblage of early Neogene and Paleogene forms found within the MTC, as might be associated with a reworked deposit. I use this turn-over in nannofossil assemblage as one criteria for defining the top of the MTC. In this study, I define both a sedimentary and biostratigraphic top from the core. The sedimentary top of the deposit marks the transition from sediment that is clearly slumped or tilted in the core and appears to have been affected by syn-depositional deformation (Figs. 3 and 4) while the biostratigraphic top, ~30 meters deeper in the stratigraphy, represents the transition from reworked into pristine nannofossil assemblages. The difference in depth is significant and could represent continued

slumping and reworking of recent sediments after the initial emplacement of the main MTC body. The biostratigraphic top is only defined at Site U1456.

The base of the complex is easily established in both drilling sites, being marked by the presence of carbonate breccias immediately overlying fine-grained sediments (Figs. 3 and 6). The depth of this contact is 1101.65 and 1054.1 mbsf at Sites U1456 and U1457, respectively. A key observation is that in the thicker Site U1456 section there is a 20-m-thick interval in which normal hemipelagic sedimentation was briefly reestablished, based on the lack of reworking in the nannofossil assemblages. This hemipelagic interval spans from around 935 to 956 mbsf (Figs. 3 and 5). This indicates that the MTC must have been emplaced in at least two phases, separated by a pause, despite the fact that this is not apparent in the seismic image. Surprisingly, the top of this hemipelagic hiatus in mass wasting is not marked by a fresh influx of clearly reworked brecciated material. Much of the hemipelagic interval comprises massive or parallel-laminated mudstones with a couple of medium-bedded massive sandstones representing less than 10% of the section (Fig. 5A). This is only moderately different from the material which lies above the hemipelagic layer, which is characterized by mudstones interbedded with thin beds of siltstone. Above the hemipelagic layer, however, there is clear evidence for slump folding, tilted bedding and microfaulting which testifies to the redeposited character of these sequences, as well as the mixed nannofossil assemblage. It is only in the somewhat shallower part of the section at Site U1456, however, that we see evidence for a fresh influx of very coarse redeposited carbonate debris flow material, above 874.2 mbsf (Fig. 3A).

(A) Site U1456



(B) Site U1457

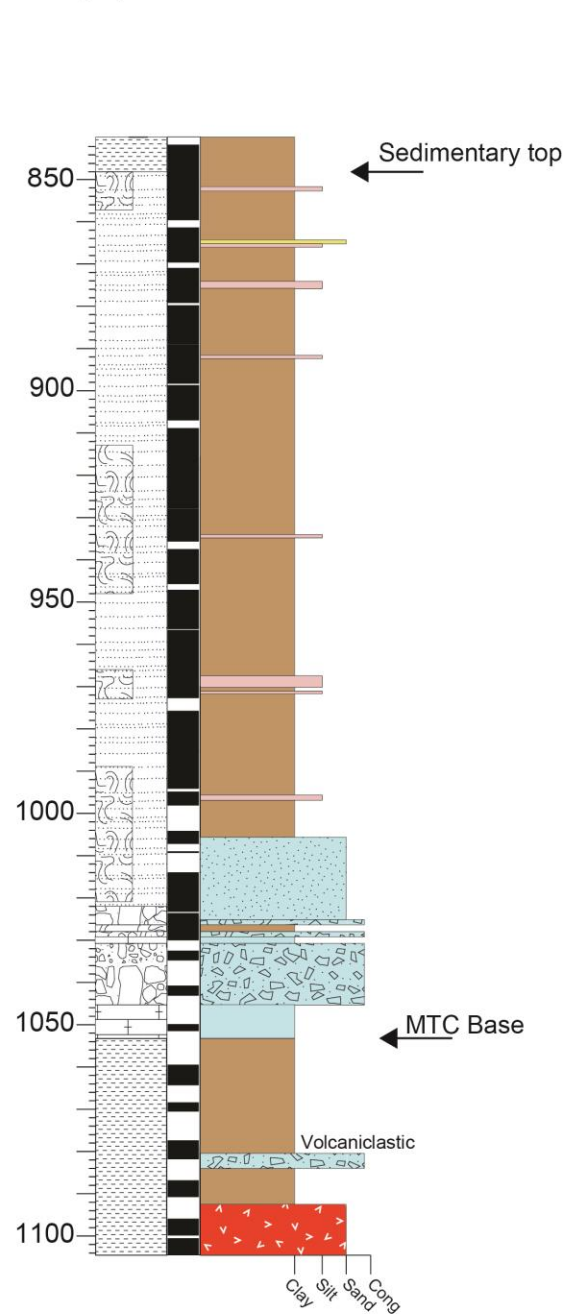


Figure 3. Summary stratigraphic columns showing the lithologies and interpreted facies of the MTC at (A) IODP Site U1456 and (B) IODP Site U1457.

At both sites, the topmost part of the deposit largely comprises fine-grained, bioturbated claystones and clay-rich siltstones, which are otherwise hard to distinguish from the background deposits of the Indus submarine fan, especially when they are not deformed. Tilted bedding is suggestive of deformation but might be interpreted as being coring related. The presence of slump folds close to the sedimentary top of each drilled section is, however, more conclusive in demonstrating continued mass wasting above the coarser grained basal units.

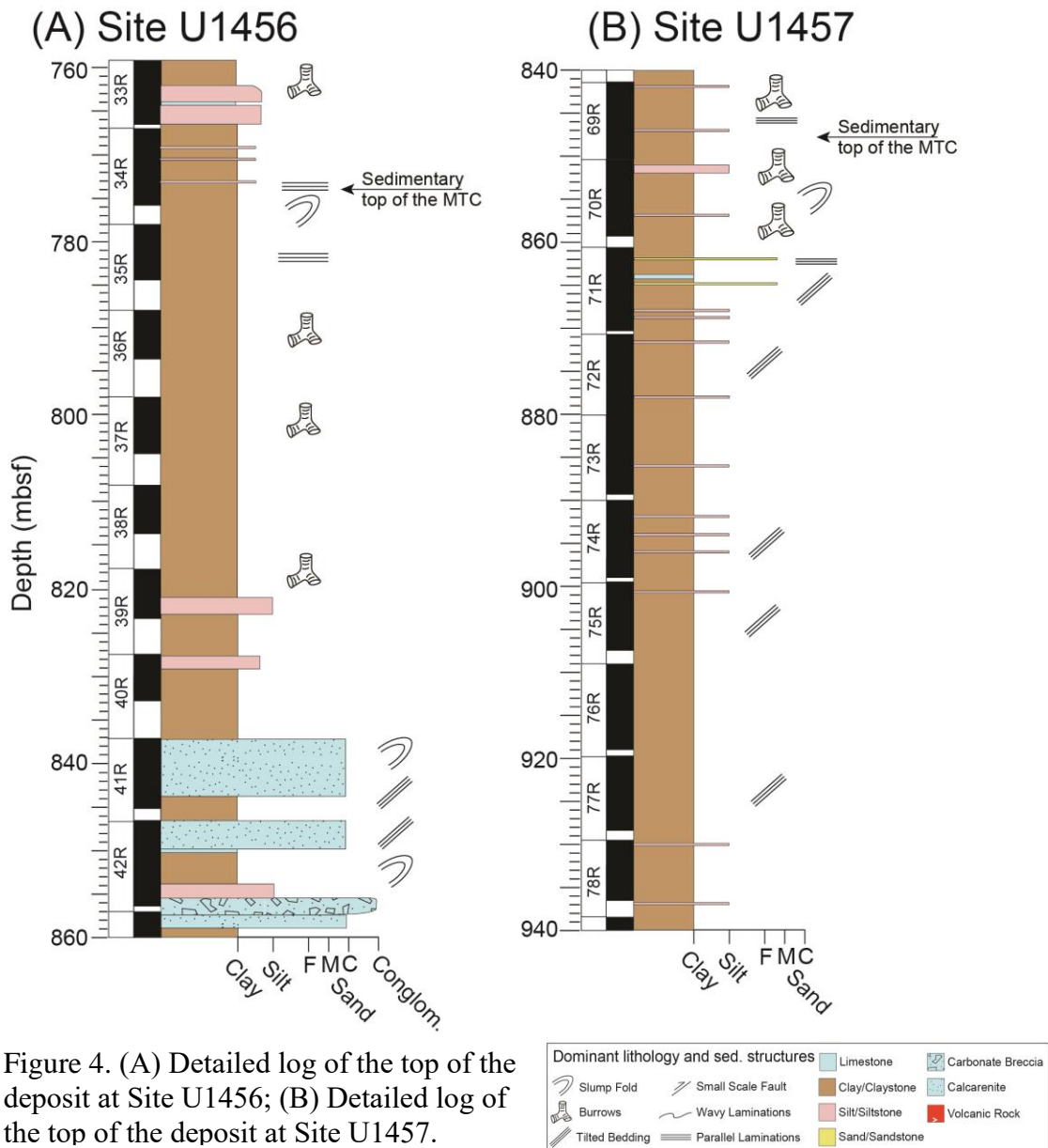


Figure 4. (A) Detailed log of the top of the deposit at Site U1456; (B) Detailed log of the top of the deposit at Site U1457.

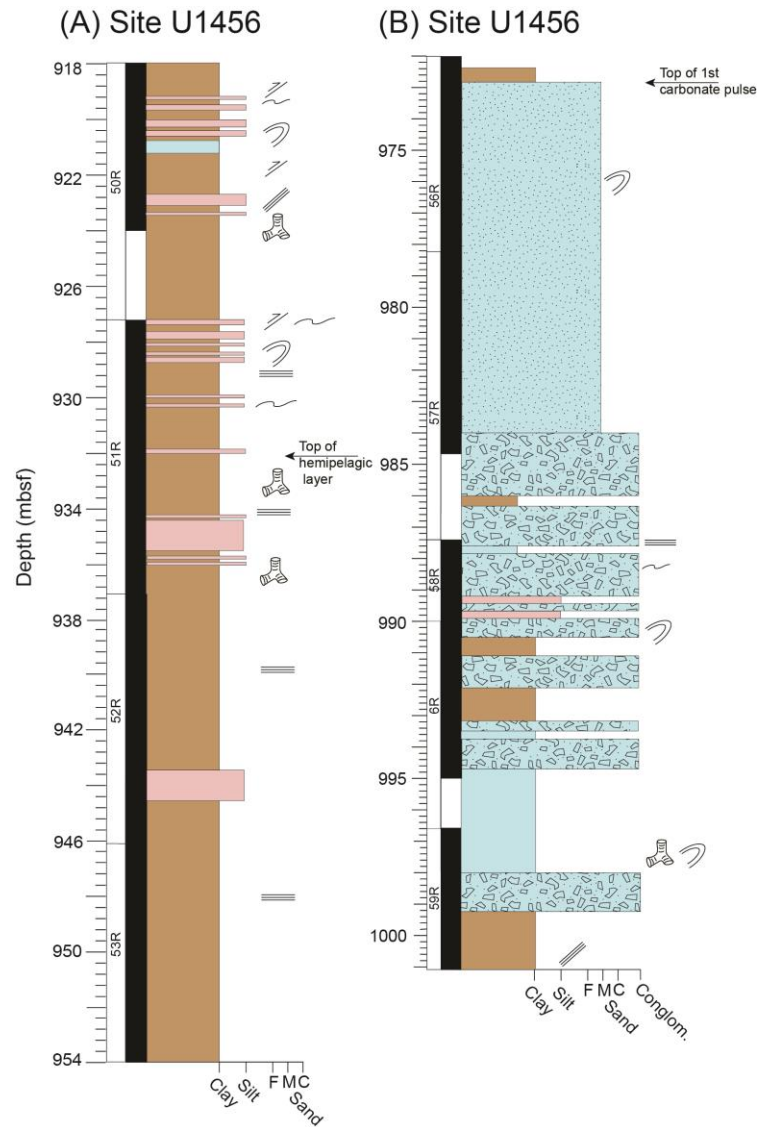


Figure 5. (A) Detailed log showing the deposit above and within the hemipelagic layer; (B) Detailed log showing the first brittle pulse of carbonate material.

4.2 Lithologic logs

Four major lithologies can be identified from the cores and are described further below: (1) Limestone, (2) Carbonate Breccia, (3) Calcarenite, and (4) Mudstone. The sedimentary structures found in the Nataraja Slide include folds, tension faults, burrows, slickensides, load structures, inverse grading, and parallel, tilted, and wavy laminations.

The top sections of the cores at both sites are dominated by a massive, siliciclastic claystone with few interbedded siltstone laminations (Fig 4). These sections are characterized by folds, reverse micro-faults, steeply-dipping laminations, and are highly bioturbated. At Site U1456, beginning at ~835 mbsf, the second pulse of carbonate material is present (Fig. 4A). This section of the MTC is dominated by few very well-sorted calcarenite units and includes few thin siltstone beds. The contacts between units are sharp and only in a few areas does the calcarenite show some graded bedding (857 mbsf). Reworked claystone underlies the carbonate section until ~935 mbsf where the hemipelagic sedimentation unit begins (Fig. 5A). The hemipelagic unit consists of massive claystone with no soft-sedimentary deformation. Some horizontal laminations with few sandy beds are present. Underlying the hemipelagic layer is ~11 meters of the claystone with few interbedded siltstone laminations. The first carbonate pulse at Site U1456 begins from ~975 mbsf and continues throughout the core to the bottom of the deposit at 1105 mbsf (Fig. 5B, 6A). This unit consists of packages of calcarenite overlying carbonate breccia and interbedded claystone no thicker than 8 meters (Fig. 5B, 6A). Sedimentary structures towards the bottom of the deposit, at both sites, include folds and trace fossils in claystone clasts (Fig 6A, 6B). At Site U1457, twenty meters of carbonate breccia, underlain by a thin limestone block, and few breccia layers, defines the bottom of the deposit (Fig 6B). Below the bottom of the MTC at Site U1457, is Paleocene claystone and volcanic material.

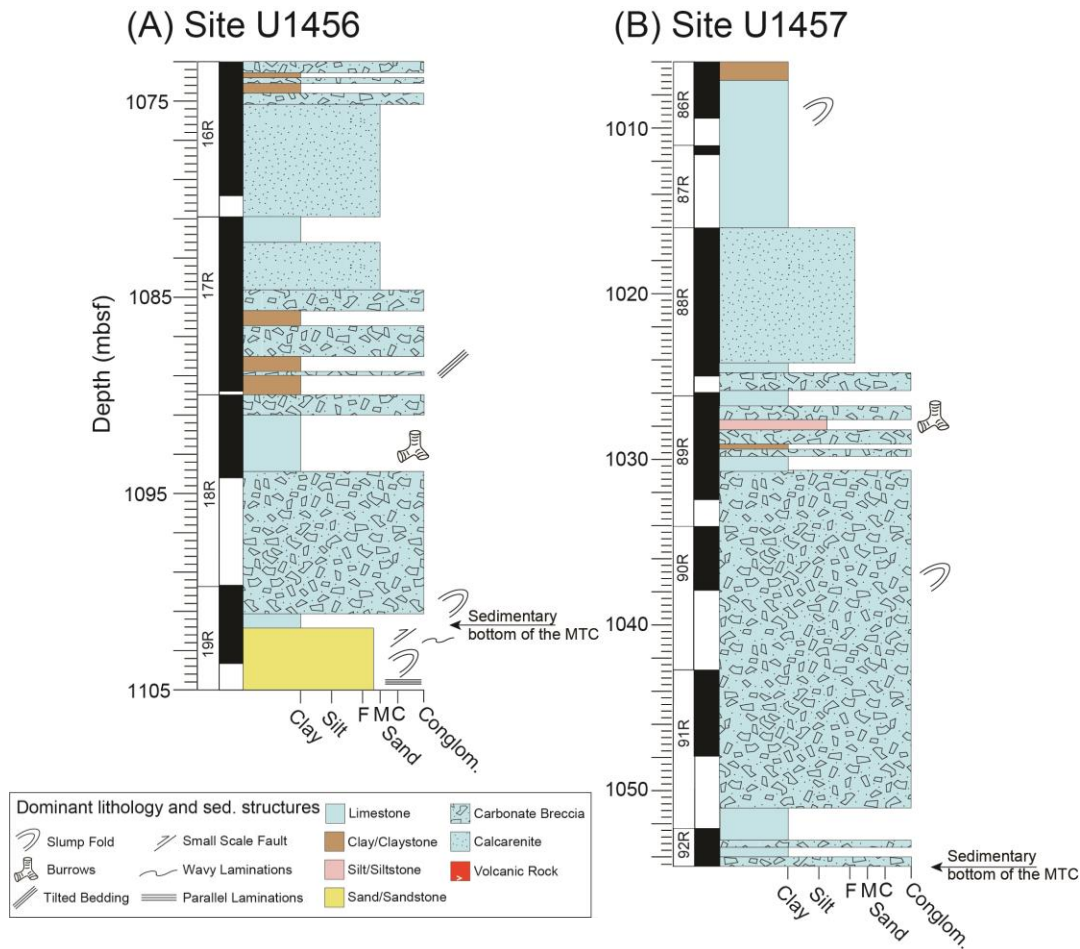


Figure 6. (A) Detailed log showing the bottom of the deposit at Site U1456; (B) Detailed log showing bottom of the deposit at Site U1457C.

4.3 Sedimentary Facies

The sedimentary facies within the MTC were determined on the basis of all descriptions and, in particular, the analysis of sedimentary structures that gives clues to the depositional processes that were operating during the emplacement of the complex. I here describe the major sediment types and provide interpretations of the depositional mechanisms. These are summarized in Figure 3.

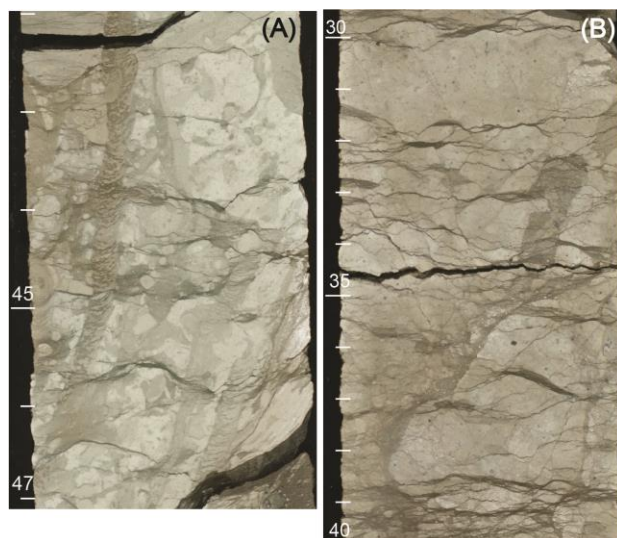


Figure 7. (A) Limestone with *Zoophycos* (20 cm long), Site U1456 (1045 mbsf); (B) Stylolite in limestone, Site U1456 (1030 mbsf).

4.3.1 Limestones

Short intervals of the MTC comprise coherent sections of fine grained limestone that show little evidence for any high-energy reworking depositional processes.

Limestones are found at Site U1456 within the lower part of the section around 1050 mbsf depth (Fig. 3). The limestones are characterized by massive and generally fine-grained micrites with moderate amounts of clay that give them an off-white color. Figure 7A shows a heavily bioturbated example with some vertical *Zoophycos* trace fossils, which are typical of sedimentation at moderate deep water, often close to the shelf edge (Ekdale, 1984; Seilacher, 1967). Figure 7B shows a massive micritic limestone with some indications of bioturbation that has also been partly recrystallized along stylolites, which are highlighted by thin clay-rich partings. Neither deposit gives any indication of strong current activity, such as ripples or laminations, but rather gentle sedimentation in a carbonate-rich environment, probably below storm-wave base. Short intervals of limestone are also found at Site U1457, very close to the base of the MTC

~1050 mbsf. These are granular and porous in character and may be the product of higher energy sedimentation in relatively shallow water depths (<30 m). Again, the limestones are tan colored rather than being pure white indicative of a modest clay content. Given the current significant water depth I propose that these limestones represent coherent blocks of relatively shallow water material that have been emplaced within the brecciated units towards the base of the MTC.

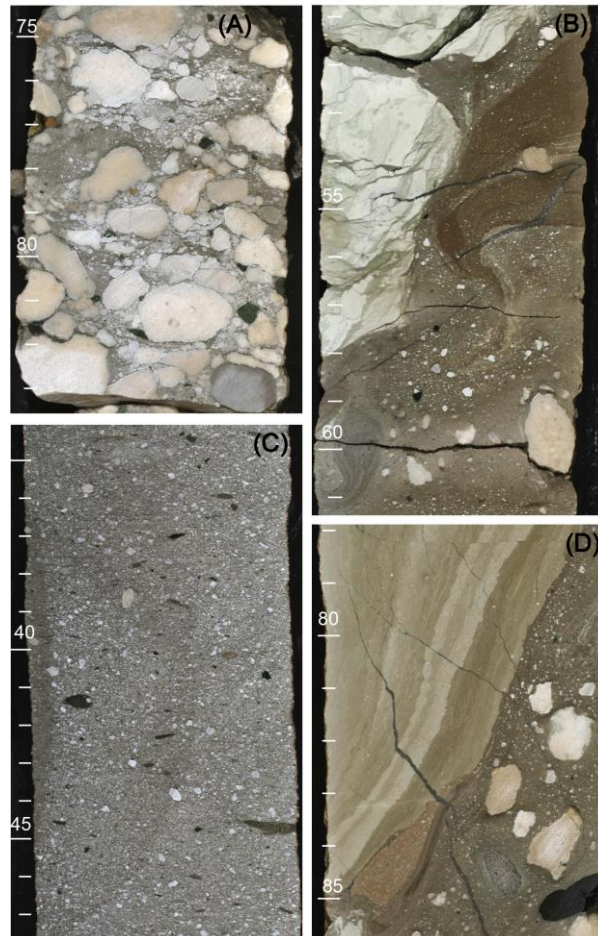


Figure 8. (A) Clast-supported carbonate breccia, U1457C (1036 mbsf); (B) Matrix-supported breccia with mud injection and slumping, U1456E (1045 mbsf) (C) Coarse sandy, debrite, U1457C (1022 mbsf) (D) Debris flow breccia with faulted mudstone raft, U1456E (1021 mbsf).

4.3.2 Carbonate Breccia Debrites

The vast majority of the carbonate sediment in the MTC is in the form of clasts in breccias, which are found mostly in the bottom parts of the deposit at both Site U1456 and U1457, with limited volumes in the upper part of the MTC at Site U1456 (Fig. 3). These breccias are thick-bedded, ranging close to 20 m thick for individual beds separated by finer grained units. At Site U1456, we see multiple such breccia units stacked on top of each other, preferentially developed towards the base. These are sometimes overlain by calcarenites (described in section 4.3.3) or by mudstones with a sharp boundary between the two lithologies. The breccias are extremely poorly sorted and the individual clasts are angular to sub-angular in character. Sizes range up to the width of the core (>10 cm). There is usually no trend towards fining or coarsening upwards within individual units, although a coarsening upwards sequence is seen in Section U1456D-43R-1 (860 mbsf). The fabric of the sediment is rarely clast supported (Fig. 8A) but is normally suspended in a dark muddy matrix (Fig. 8B and 8D).

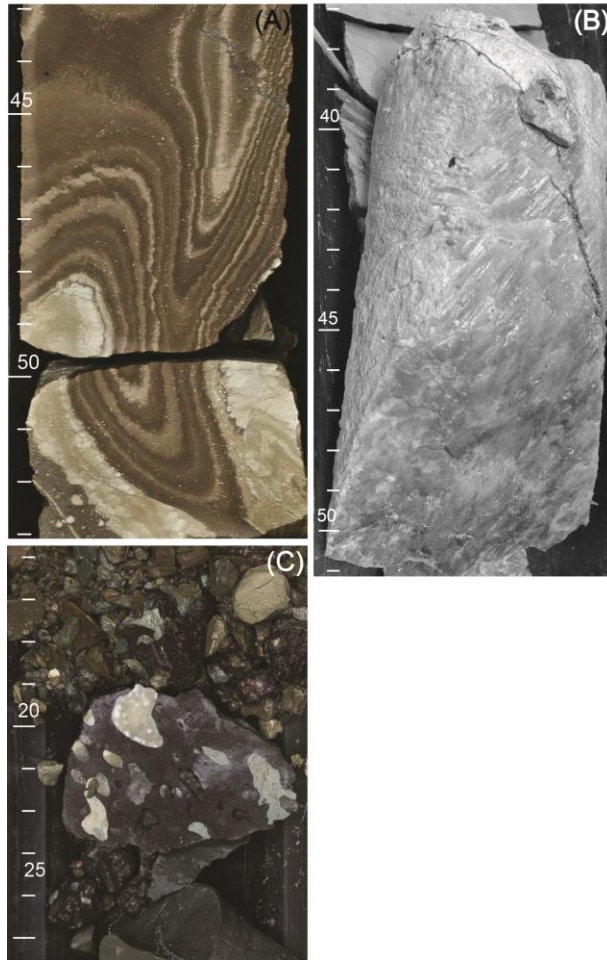


Figure 9. (A) Slump folded calcareous siltstone, U1456D (989 mbsf) (B) Slickenside marks on a fault within silty claystone, U1456E (1021 mbsf); (C) Deccan vesicular basalt clast, U1456D (879 mbsf).

The limestone clasts themselves are pale tan or bright white with the interior showing very fine-grained or slightly granular sediment classified as micrite or packstones {Dunham, 1962 #147}. In the very densest part of the beds (~1036 mbsf at Site U1456), clasts are seen to indent one another as a result of dissolution during diagenesis and this is visible both in core surfaces (Fig. 8A) as well as in microscope thin sections, described in more detail below (Fig. 12D).

Most of the carbonate breccia debris flows are extremely poorly sorted, but are sometimes in the form of sorted, coarse, sandy debrites devoid of larger clasts (Fig. 8C). These larger granular clasts are supported in a muddy sandstone matrix with no clear grading within the unit. The vast majority of the carbonate rocks redeposited in the debris flows appear to have been lithified prior to their resedimentation, because as well as angular clasts, we see coherent rafts of sediment, tens of centimeters across floating within finer grained units (Fig. 8D). However, some of the carbonate sediment must have been unlithified during emplacement, as locally we can see soft sedimentary folding of the deposits, such as seen in muddy limestones (Fig. 9A). These are not common throughout and represent a relatively small part of the total sequence. It is clear that brittle deformation is important locally, especially between and within the more coherent carbonate blocks that even include slickensides, (Fig. 9B) testifying to rapid brittle deformation of the carbonate rocks during their emplacement. Although limestone fragments dominate the debris flows, it is noteworthy that locally there is evidence for volcanic reworking. These clasts are weathered, red-brown stained in their appearance and have a sub-rounded character. The largest single clast was found at 879 mbsf, within a poorly solidified conglomeratic part of the debris flow sequence, and is an 8-cm-wide vesicular aphyric basalt, presumed to be derived from the Deccan Plateau sequences onshore (Fig. 9C).

The limestone, from which the clasts were derived from, formed as a typical shallow-water deposit in a biologically productive zone starved of clastic sediment input. Original water depths were likely within the photic zone on the continental shelf (<50 m), with only moderate amounts of current activity as there is see no obvious evidence

for strong sorting or high energy deposits such as oolites or grainstones. These original deposits have been reworked as debris flow deposits during the emplacement of the MTC. The muddy matrix has a separate provenance, either from the deep-water slope of peninsular India or from the Indus Fan itself, as discussed below.

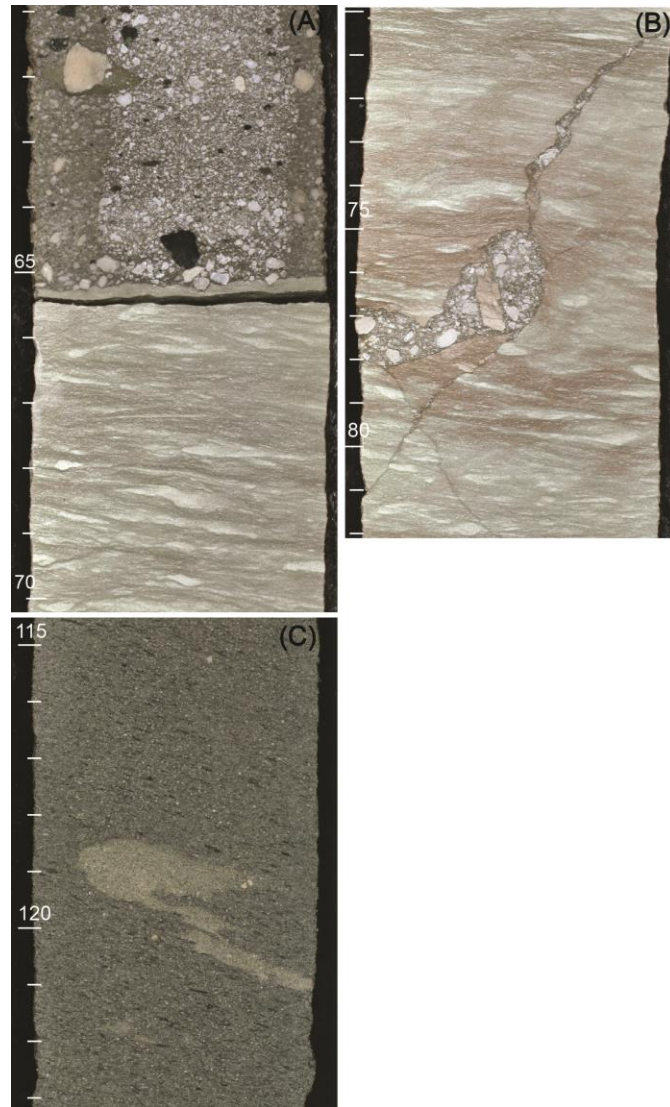


Figure 10. (A) Sharp contact between calcarenite and calcareous siltstone, U1457C (1025 mbsf); (B) Dike of breccia cutting through calcareous siltstone, U1457 (1025 mbsf) (C) Massive calcarenite with ductile folded layer U1456D (841 mbsf).

4.3.3 Calcarenites

Calcarenite is present in each carbonate section, as a massive, well-sorted unit suggesting of high energy current transport. Beds of the calcarenite are several meters thick and generally massive in structure, although they commonly develop a sub-horizontal fabric suggestive of current flow. Where the deposits are finer, (Fig. 10A, 10B) there is a shear-type fabric developing within calcareous siltstones. In the coarser grained units, (Fig. 10C) there is some evidence for internal soft sedimentary deformation, although generally the units are homogenous and comprise uniform, gray, coarse-grained sandstone. They are generally well sorted and clast supported with very little muddy matrix, suggestive of a high energy depositional regime. The vast majority of the clasts are composed of carbonate, although there are a significant number of dark grains of organic carbon origin. These beds often have sharp tops, which we interpret to reflect erosion of the deposit prior to the emplacement of the overlying unit. Figure 10A shows a calcareous siltstone sharply overlain by a coarse-grained debrite deposit. Very few sedimentary structures are seen within these deposits, inferring sedimentation in an upper flow regime, resulting in relatively laminar deposits without any current ripples or

finer interbeds. Sediment concentrations was assumed to be very high during deposition which appears to have terminated rapidly.

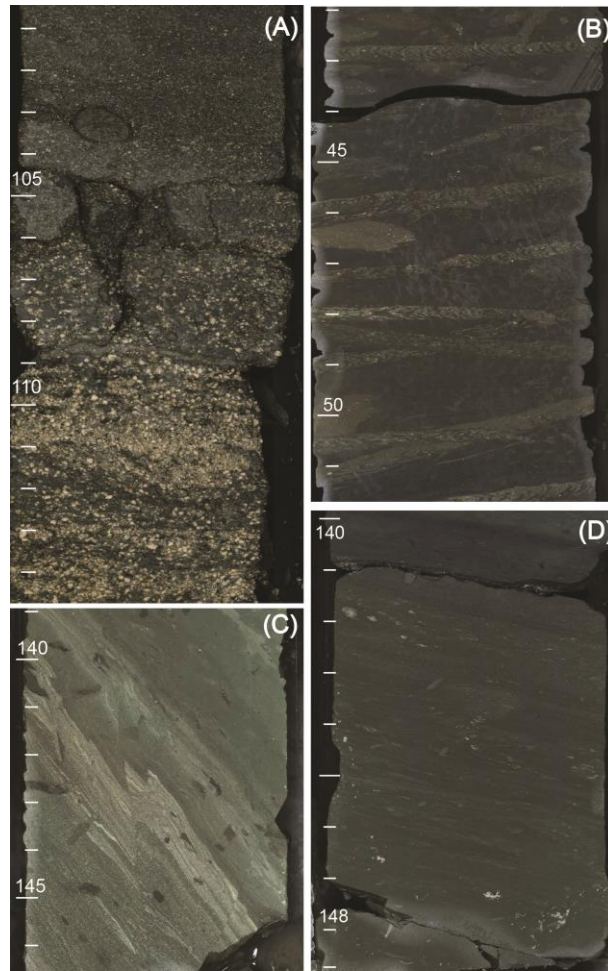


Figure 11. (A) Sandy siltstone showing gradual normal grading, U1457C (865 mbsf); (B) Mudstone with burrows, U1457C (832 mbsf); (C) Steeply dipping laminated mudstone showing reverse faulting, U1456D (883 mbsf); (D) Tilted, laminated turbidite deposit U1457C (881 mbsf).

4.3.4 Turbidites and Hemipelagic Mudstones

Apart from the carbonate-dominated debris flows, minor turbidite sandstones and dominant siltstones and mudstones make up the single largest part of the MTC. These are also interbedded with their associated hemipelagic mudstones. In the coarsest sections, the turbidites show classic fining upward sequences (Fig. 11A) with the largest fragments

still composed of carbonate grains floating within a darker, clastic mud matrix. Locally, sub-horizontal laminations are present, although generally sedimentary structures are poorly developed with up-section grading dominating these deposits. In the upper parts of the MTC, at both sites, the muds show lamination and interbedding of modest amounts of muddy silt (Fig. 11D). Elsewhere, the deposits are massive, dark gray mudstones with few sedimentary structures. These contrast with the mudstones that overlie the MTC where typical deep-water trace fossil assemblages, e.g., *Zoophycos* (Fig. 11B) characterize the hemipelagic sedimentation and eliminate the possibility of large-scale mass wasting. This is also different from the muddy tops of the MTC itself, where there is evidence for laminar current flow that follows the initial emplacement of the debris flow deposits at the base of each cycle. In general, the grain sizes are relatively limited with only few thin-bedded sandstones and occasional siltstones developed within what is otherwise a dominantly (95%) muddy sequence. Distinguishing these from the hemipelagic interval within Site U1456 is difficult without the help of micropaleontology evidence.

Syn-depositional deformations within the muddy turbidities include folds, micro-faults, and steeply tilted bedding (Fig. 11C). The structures are particularly easy to see in well laminated sequences and dips can be high, more than 50°, from horizontal indicating significant deformation of the muddy units after sedimentation. As well as slump folds, there is evidence for brittle faulting often of a compressive high-angle character, usually in the form of thrusts. Significant dips and deformation is evidence for incorporation as part of the MTC, rather than the subsequent hemipelagic sedimentation of the Indus submarine fan.

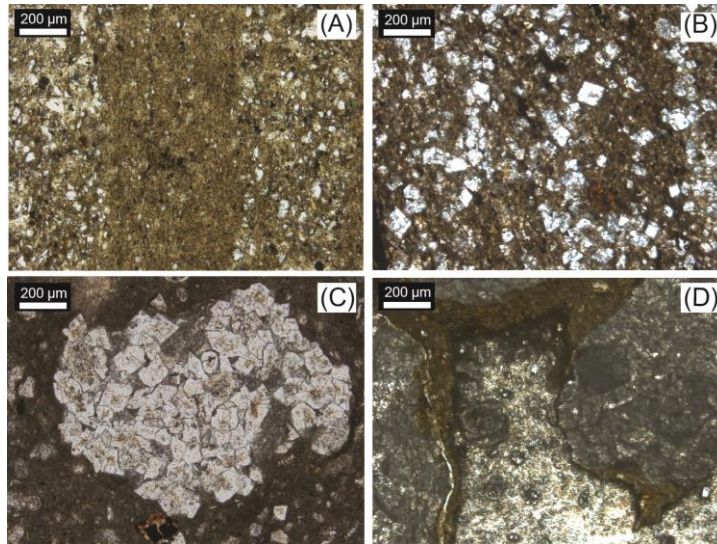


Figure 12. Thin Sections- plane polar (A) Laminated sandy siltstone with euhedral quartz grains, U1457C (997 mbsf); (B) Calcarenite, U1456D (1006 mbsf); (C) Euhedral calcite/dolomite crystals within larger grain, U1456E (1073 mbsf); (D) Suture grain contact of carbonate clasts in breccia, U1456D (870 mbsf).

4.4 Microscopic Facies

Microscopic analysis of thin sections provides an overview of the facies present in the cores to help interpret paleoenvironment and depositional mechanisms. Figure 12A shows a silty laminated mudstone present in the upper part of Site U1457, interpreted as a turbidite deposit. Note the finer muddy center of the slide and the poorly sorted silt interbeds on either side with dominant quartz clasts. The massive calcarenite beds that overlie debris flow deposits are seen to be relatively poorly sorted and matrix supported, at least local, in thin section (Fig. 12B). The clasts are seen to be calcite crystals and a variety of finer limestone microfacies, especially micrite. The carbonate breccias themselves are dominated by shallow-water facies as described above, but there are also aggregates of dolomite crystals suggestive of redeposition from shallow water areas (Fig. 12C). I interpret these aggregates to represent diagenetic alteration

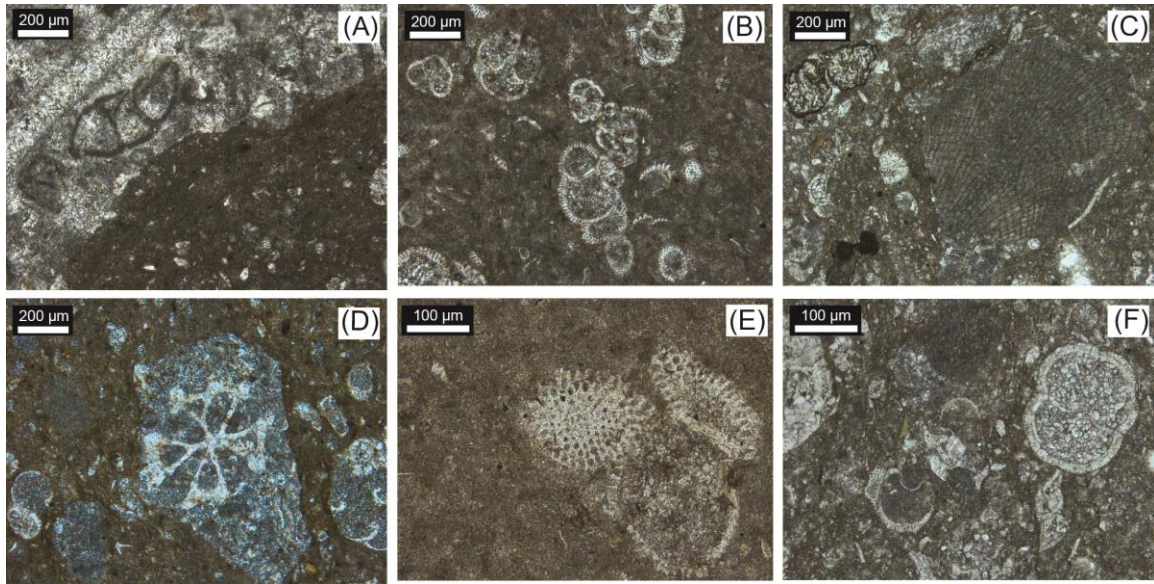


Figure 13. Thin Sections- plane polar (A) Uniserial benthic foraminifer in breccia clast, U1456E (1073 mbsf); (B) Siltstone with planktic foraminifers, U1456D (989 mbsf); (C) Bryozoan and foraminifers in carbonate breccia, U1457C (1035 mbsf); (D) Echinoderm spine in carbonate clast, U1456D (1017 mbsf); (E) Radiolarian showing pore structure in siltstone, U1456D (989 mbsf); (F) Planktic foraminifers and bioclasts in carbonate breccia, U1457C (1035 mbsf).

of original calcite via interaction with magnesium-rich waters prior to resedimentation. In few areas throughout the MTC, where the carbonate breccias are clast supported, suture contacts are formed from compaction during deposition, and dissolution post-burial (Fig. 12D).

Microscopic investigation highlights the biogenic character of the original carbonate deposits. There are large numbers of microfossils and their fragments within the limestone clasts. Foraminifers are abundant (Figs. 13A, 13B, 13F). In addition, we also see evidence for the presence of crinoid fragments (Fig. 13D), bryozoans (Fig. 13C) and rare radiolarians (Fig. 13E).

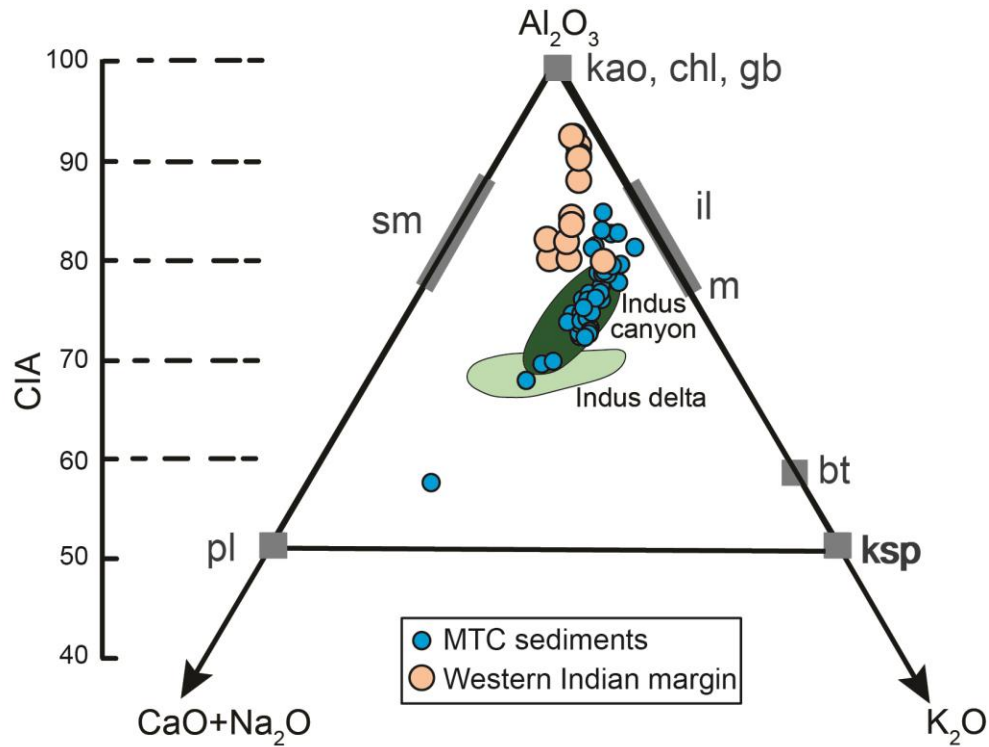


Figure 14. (A) Geochemical signature of the analyzed samples illustrated by a CN-A-K ternary diagram (Fedo, 1995). CN denotes the mole weight of Na_2O and CaO^* (CaO^* represent the CaO associated with silicate, excluding all the carbonate). A and K indicate the content of Al_2O_3 and K_2O respectively. Samples closer to A are rich in kaolinite, chlorite and/or gibbsite (representing by Kao, Chl and Gb). Chemical Index of Alteration (CIA) values are also calculated and shown on the left side, with its values correlated with the CN-A-K. Abbreviations: sm (smectite), pl (plagioclase), ksp (K-feldspar), il (illite), m (muscovite), bt (biotite).

4.5 Geochemistry

4.5.1 Bulk Geochemistry

I use a CN-A-K ternary diagram to illustrate the geochemical character of the analyzed sediment and to compare this to the sediment from the Indus canyon and delta. The sediment from the MTC largely plots within the range of the Indus canyon and trends towards higher values of Al_2O_3 (Fig. 14A). They appear to have higher values that trend towards illite end-members and are more depleted in biotite and feldspars, likely a result from sediment transport, as also seen in the Indus Canyon (Li et al., 2018). The few

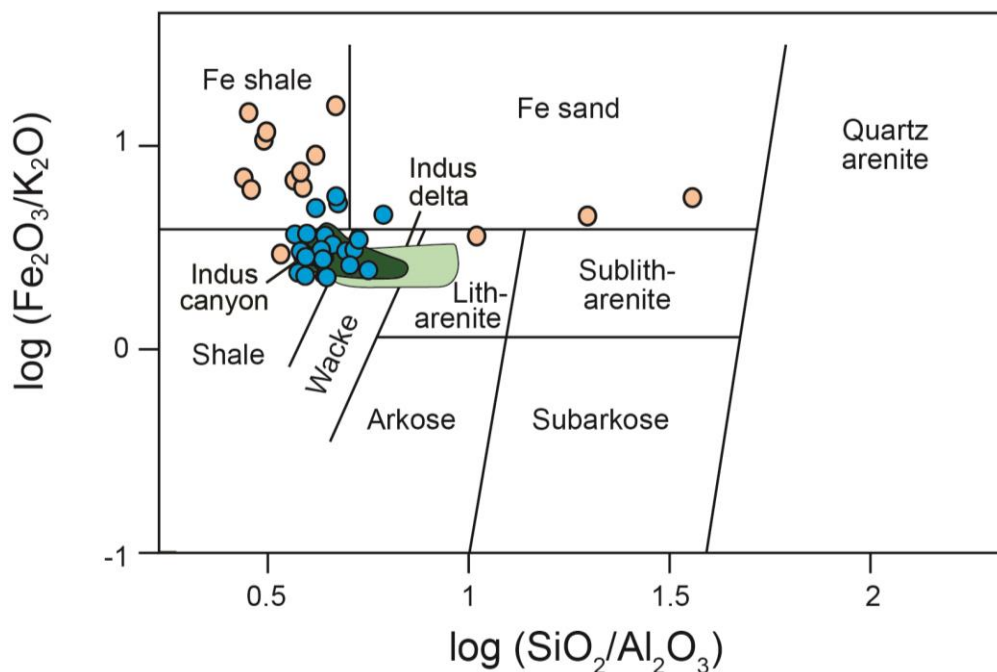


Figure 14. (B) Geochemical classification sediments from the Indus delta (Clift et al., 2010), Indus Canyon (Li, 2018), and shelf sediments from the Indian margin (Kurian, 2013) following the scheme of Herron (1988).

samples that plot below the signature of the Indus canyon may be the result of small amounts of carbonate left after decarbonating. The MTC sediments show moderate overlap with the shelf sediment from the western Indian margin, largely derived from rivers draining the Deccan Plateau (Kurian et al., 2013).

The sediment in the MTC can also be characterized using other major element discrimination diagrams. Figure 14B shows the scheme of Herron (1988) in which the samples largely plot within the wacke and shale field, with a few slightly more rich in Fe. The samples also show a preference of lower silica. Again, we plot these samples along with the Indus canyon and delta sediment. They form a cluster within the range of the Indus canyon sediment, suggesting provenance of reworked Indus material. Comparison with sediment from the western Indian margin show a significant

difference, with the shelf sediment typically plotting with much higher Fe contents. I infer only limited amounts of the clastic sediment can be derived from the Indian margin.

4.5.2 Neodymium and Strontium Isotopes

I use the Sr and Nd isotopes to constrain the provenance of the clastic sediment in the Nataraja Slide. Cross plotting these isotopes against one another and with known compositions of source regions such as the Deccan Traps, Transhimalaya, Karakoram, Greater Himalaya, Kirthar and Sulaiman Range, and modern/Quaternary Indus-derived sediment allows the origin of the sediment to be constrained (Fig. 15). This diagram shows that the MTC samples form a relatively discrete cluster with one exception that has especially positive ϵ_{Nd} values that fall within the Deccan and Transhimalayan arrays. When comparing these data with potential sources and other sediments, it is clear that the bulk of the sediments lie within the isotopic range defined by modern submarine fan sediments at the same drilling sites, consistent with the idea

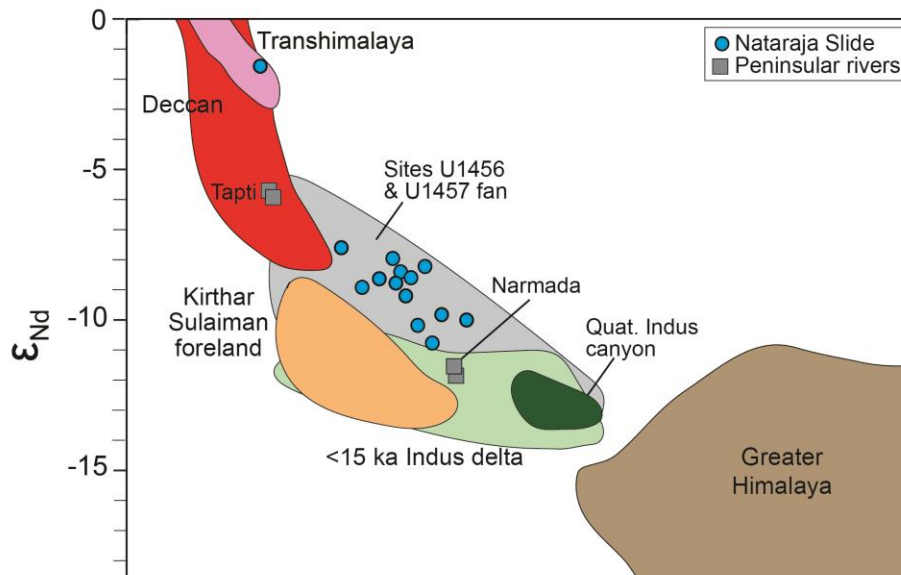


Figure 15. Cross plot of strontium versus neodymium isotope data from the MTC showing the relationship with other sediments within the submarine fan at these drilling locations as well as major source regions onshore and the modern Mahi, Tapti and Narmada River sediments (Goswami et al., 2012). Kirthar and Sulaiman data is from Zhuang et al. (2015)

that much of this material may be reworked Indus-derived sediment. However, it is impossible to exclude mixing of sediment from the Tapti or Narmada Rivers. These isotopes do not allow the ability to quantify the degree of reworking from these sources. Although the samples plot with higher ϵ_{Nd} values compared to the Quaternary Indus and its canyon, as well as the onshore ranges of the Kirthar and Sulaiman, such a departure can largely be explained through the temporal variations in the Indus itself (Clift, 2005; Clift, 2018). The one very positive ϵ_{Nd} sample is however anomalous and plots with even more positive values compared to the

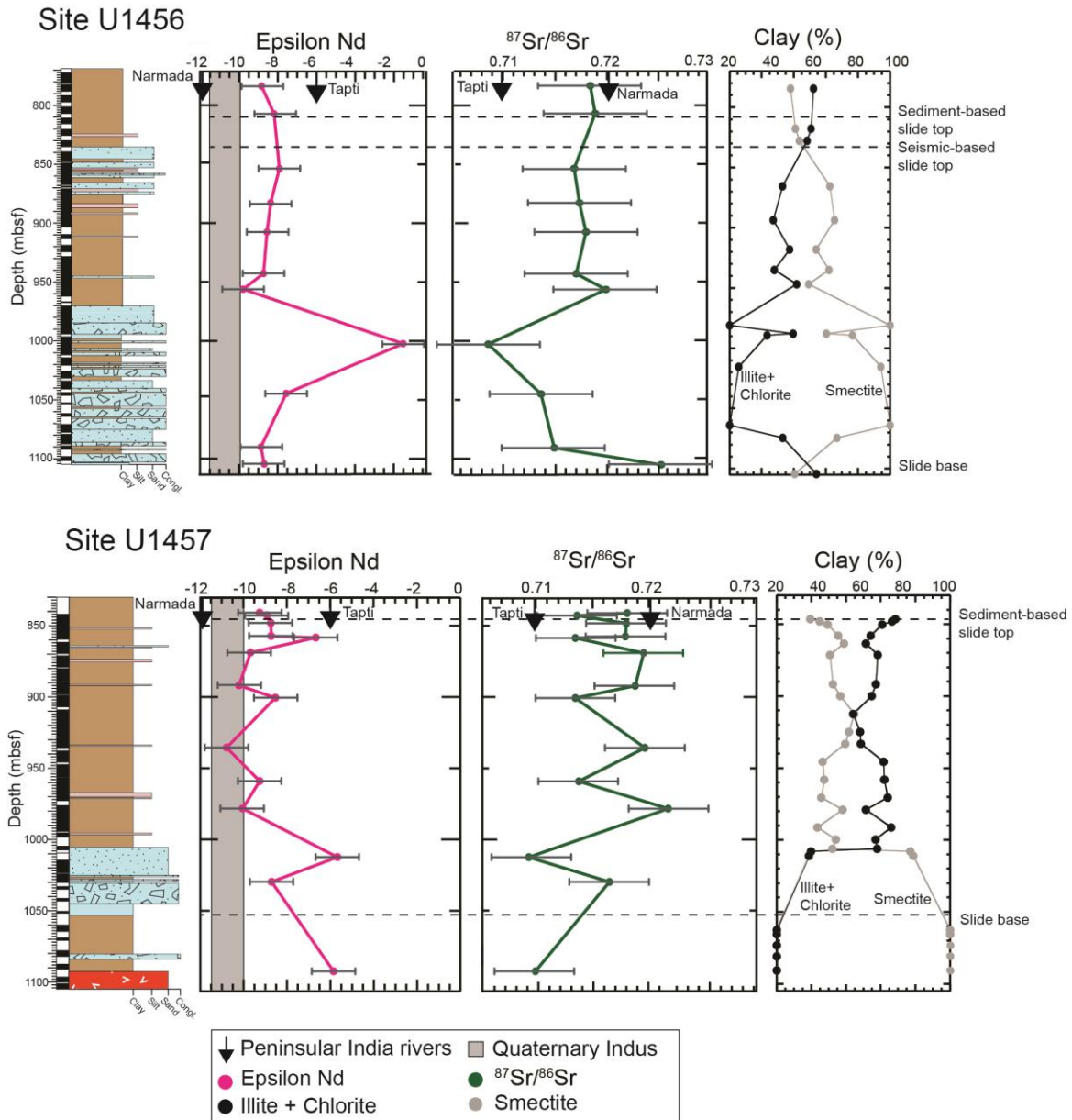


Figure 16. Downhole plots of Nd and Sr isotope composition and clay mineralogy of the decarbonated sediment at IODP Site U1456 and Site U1457. Gray vertical bar shows compositional range of Quaternary sediments in the Indus Delta (Clift et al., 2010; Clift, 2008), as well as modern Tapi and Narmada River sediments (Goswami et al., 2012).

Tapti River. This is strongly suggestive of erosion from peninsular India and is consistent with the presence of vesicular Deccan basalt fragments, as noted above.

I also look at the stratigraphic variation in these isotopes by plotting them next to the sedimentary columns for each section (Fig. 16). In both cases the neodymium isotopes plot slightly more positive ϵ_{Nd} values or within error of the Quaternary Indus, but it's noted that the most positive ϵ_{Nd} values in each borehole are found within the debris flow breccia units at the base of the lower unit of the MTC. This is especially true at Site U1456. Variations in the $^{87}Sr/^{86}Sr$ also mirror this general evolution. The provenance of the coarse grained debris flow deposits is different from those of the finer grained sediments overlying. The fine-grained sediments may represent recycling of pre-existing fan sediments into the top of the MTC, while the debris flow deposits are more closely associated with mass wasting from the western Indian continental margin.

4.5.3 Clay Mineralogy

The clay mineral assemblages within the MTC can be used to assess provenance through comparing the semiquantitative analyses with existing data from other sources. When the data is plotted on the ternary diagram of illite+chlorite, kaolinite and smectite, (Fig. 17) there is significant overlap between the new MTC data and other Arabian Sea sediments (Rao and Rao, 1995). In general, the MTC clays are very low in kaolinite and form an array between the smectite and illite+chlorite end members. In this respect, they show a similar behavior to sediments from the Indus fan, and also have significant overlap with clays from the Indus Canyon (Li, 2018). Although some of the samples have compositions consistent with erosion from the Indus shelf, with relatively high smectite contents, it's noted that the bulk of the sediments plot with

higher illite+chlorite values. They also tend to have slightly higher kaolinite compared with analyses done on sediments from the Indus floodplains on shore (Alizai et al., 2011). In general, the MTC deposits have lower kaolinite compared with most Western Indian shelf deposits, although they do plot very close to the assemblage known from the Saurashtra margin (Rao and Rao, 1995). It is also noteworthy that the MTC assemblages generally show lower illite+chlorite compared with many of the Indus submarine fan deposits, suggestive of a more chemically weathered origin. Taken together, the data indicate recycling of Indus Fan deposits, but with the possibility of involvement of clays derived from the Western Indian margin, particularly in the vicinity of Saurashtra.

The clay mineralogy shows some significant variation with depth (Fig. 16). At Site U1456 the carbonate-rich part of the section shows particularly high smectite contents and relatively low (illite+chlorite) values. Smectite only becomes less abundant than these two physically weathered clays above the upper Phase 2 carbonate debris flow unit. At Site U1457, the carbonate rich part of the section is again seen to be smectite-rich, but immediately above this level the sediments become more dominated by (illite+chlorite), similar to the rest of the Indus Fan. It is noteworthy that the Paleocene sediments under the MTC at Site U1457 are essentially 100% smectite, possibly reflecting chemical weathering of the underlying basaltic basement. The clay mineralogy thus supports the isotope data in showing a significant difference between the material within the carbonate dominated section and the mudstone dominated sequences above. I infer more Indian peninsula flux to the lower parts of the MTC.

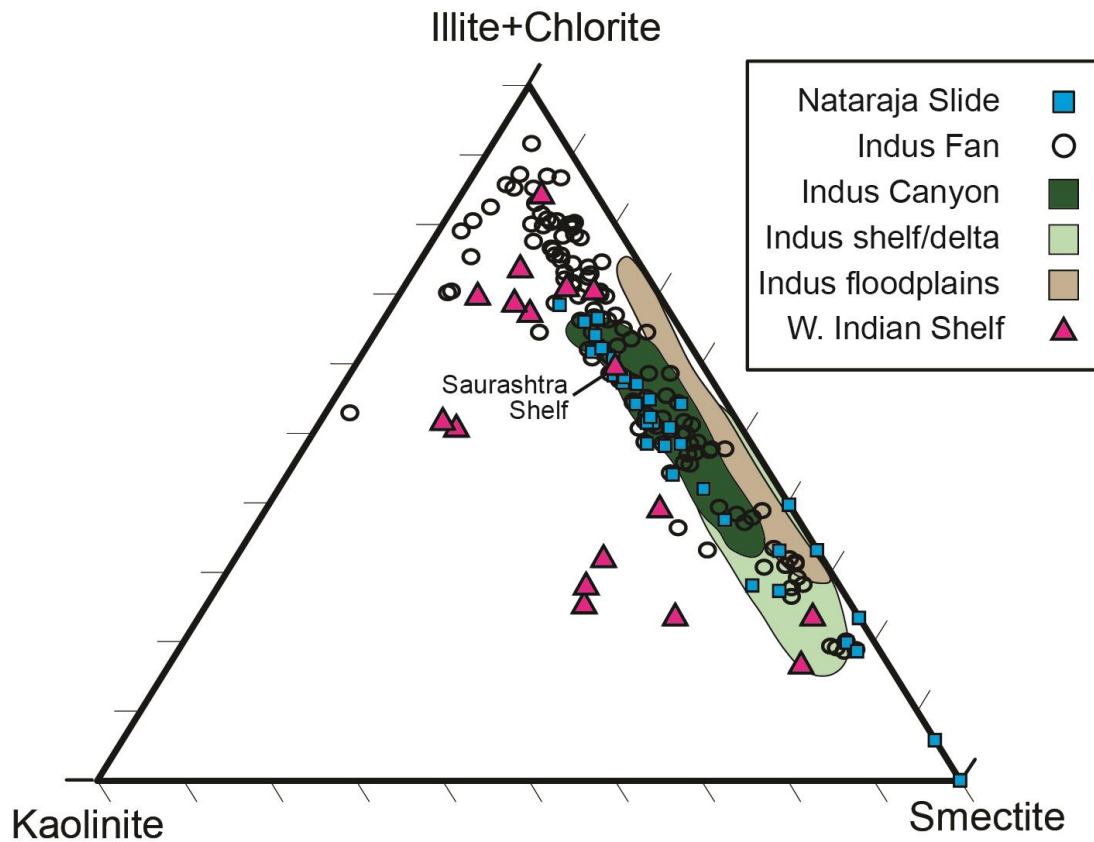


Figure 17. Ternary diagram of clay minerals from IODP Site U1456 and U1457 indicates a clay mineral assemblage consisting mostly of smectite, chlorite and illite. Clay mineral data from source regions are plotted to compare their clay assemblages. Data from western Indian shelf modern sediments are from Rao and Rao (1995), Indus canyon data is from Li (2018) Indus flood plain and delta data is from Alizai et al. (2012), and Indus Fan data is from Peng Zhou (unpublished).

5. DISCUSSION

5.1 Depositional Mechanisms

Because of the long run out distance and presence of a hemipelagic zone, the deposit is likely to have a complex transport history. Most of the sediment within the Nataraja Slide is composed either of debris flow deposits, well sorted calcarenite sandstones, or dominantly clastic turbidite siltstones and mudstones. I interpret two main phases of deposition of the MTC at Site U1456 (Fig. 3) that show a general fining upwards with a dominance of debris flow activity towards the base, and more siliciclastic turbidite sedimentation towards the top. Within the two overall fining upwards cycles at Site U1456, it is apparent that there are shorter phases of fining upwards. For example, the upper part of Phase 1 sedimentation (likely a second emplacement pulse after the initial event) comprises a basal unit from between 999.2 and 984.0 mbsf that is dominated by rafted carbonate limestone sheets and carbonate debris flow material (Figs. 3 and 5B). Above 984.0 mbsf, there is a transition to massive thick bedded calcarenite with slump folds, although this is truncated sharply at 973 mbsf, where it is overlain by mudstones that rapidly transition into the hemipelagic sedimentation break described above. This implies that the basal Phase 1 unit, especially at Site U1456, comprises a series of pulses rather than one single gigantic deposit as might have been implied by the seismic data alone (Calvès et al., 2015)(Fig.2).

Although Site U1456 is in a more central location within the basin, the oldest debris flow breccia at the base of Phase 1 is thinner in this location than at Site U1457, and transitions more rapidly up into thick-bedded breccia and interbedded calcarenites. Both sections, however, do show an overall fining upward between the base

and overlying mudstone units. The initial section of debris flow sedimentation appears to be around 94 m thick at Site U1456 (1101.6–1007.2 mbsf) and approximately 48 m thick at Site U1457 (1006.4–1054.3 mbsf)(Figs. 3 and 6).

In general, calcarenite sandstones alternate with debris flow breccias (Fig 6A) indicating an alternation of depositional mechanisms within the overall emplacement episode. Individual debris flow events are followed by high-energy upper flow regime periods of sedimentation, where massive well-sorted calcarenites are deposited before another debris flow unit, although presumably all of these units are emplaced over a relatively short period of time. The carbonate-dominated debris flows form the initial erosive base of the MTC, followed by mud-dominated turbidite sedimentation and hemipelagic fallout representing the tail of the MTC. Soft sediment deformation is commonly seen in the more laminated sections indicative of slumping after sedimentation. It seems unlikely that poorly consolidated mudstones and siltstone could have been emplaced hundreds of kilometers in a semi-coherent form, unlike the well lithified limestones seen close to the base of each section.

5.2 Triggering Mechanisms

Rapid accumulations of sedimentary deposits, a sloping seafloor, and environmental stresses are the most common conditions associated with the triggering of submarine landslides (Hampton and Locat 1996). My hypothesis is that the rapid accumulation of sediment on the Western Indian continental margin, sourced from the Indus and smaller western Indian rivers, resulted in an unstable stratigraphy that was then more liable to mass wasting. There is strong evidence that the margin is gravitationally unstable because of the observation of compressional thrusts towards the base of the

slope, seen between Saurashtra and the Bombay high (Nair and Pandey, 2018). This demonstrates gravitational collapse, which has yet to be manifest in the dramatic fashion seen in the Nataraja Slide. Sequence stratigraphic interpretation of seismic data from the Laxmi Basin show chaotic reflections representing a large increase in clastic sediments from a major transgression (Pandey and Pandey, 2015). The large increase in sediments to the margin can also be correlated with the increase in the Asian monsoon from ~24 Ma until ~10 Ma (Clift et al., 2008). A strengthening in the monsoon would have caused an increase of erosion of the Himalayas that would have resulted in an increase of sediment loading the Indian margin. This increased influx of clastic material resulted in gravity driven tectonics and growth faults that could've been the beginning of this mass failure. Additionally, the way the sediment was originally deposited on the continental slope could promote weak layers that will eventually fail.

Peninsular India is a stable continental region. However, the area is still at risk of large intraplate earthquakes (Chung and Gao, 1995). In 1819, the Kutch earthquake, with a moment magnitude of 7.8, occurred near the town of Bhuj. It was felt over an area of nearly $3 \times 10^6 \text{ km}^2$, within the area of the scarp of the mass movement described here. In 1965, a second earthquake, the Anjar earthquake, occurred very close to the previous event. Both of these events are presumed to be associated with a paleo riftzone (Chung and Gao, 1995). The northwestern margin of India is characterized by Mesozoic rifting, of which has created three rift basins; Kutch, Cambay, and Narmada (Biswas, 1989). Although records of earthquakes do not extend to the time period of the mass movements described here, this is a possible cause of the large redeposition of sediment during the

late Miocene. The observation that former rift zones are sites of midplate seismic activity, plays an important role here (Chung and Brantley, 1989).

More than likely the cause of the mass wasting was a combination of many conditions occurring during the mid to late Miocene time on the Western Indian continental margin and warrants further study and investigation.

5.3 Other Mass Movements

The processes and subsequent deposits seen in the mass movement of the Nataraja Slide can be compared to other mass transport complexes around the world. The submarine landslides on the Miocene carbonate platforms of the Luconia Province, offshore Malaysia, show prograding carbonate platforms that were oversteepened before failing (Zampetti et al., 2004). Like in the Nataraja Slide, hemipelagic muds were intermixed with the carbonate-rich slide blocks. The triggering mechanism here was attributed to active faulting in the area. Other mass transport deposits differ in that they are mostly made up of sandy material, but still show a variety of processes ranging from sliding to debris flows (Bahk et al., 2016). The popular Storegga Slide also includes processes as described here. The mass movement was entirely siliciclastic in character and was comprised of debris flows that were transported into the basin with high mobility, suggesting hydroplaning (Bryn et al., 2005). The triggering of the Storegga Slide included a combination of factors such as a glaciated margin and seismicity. The Algulhas Slump, found offshore South Africa, was also triggered from seismicity, but included slumping of the margin, and less high energy deposition, as seen in the Nataraja Slide (Dingle, 1977).

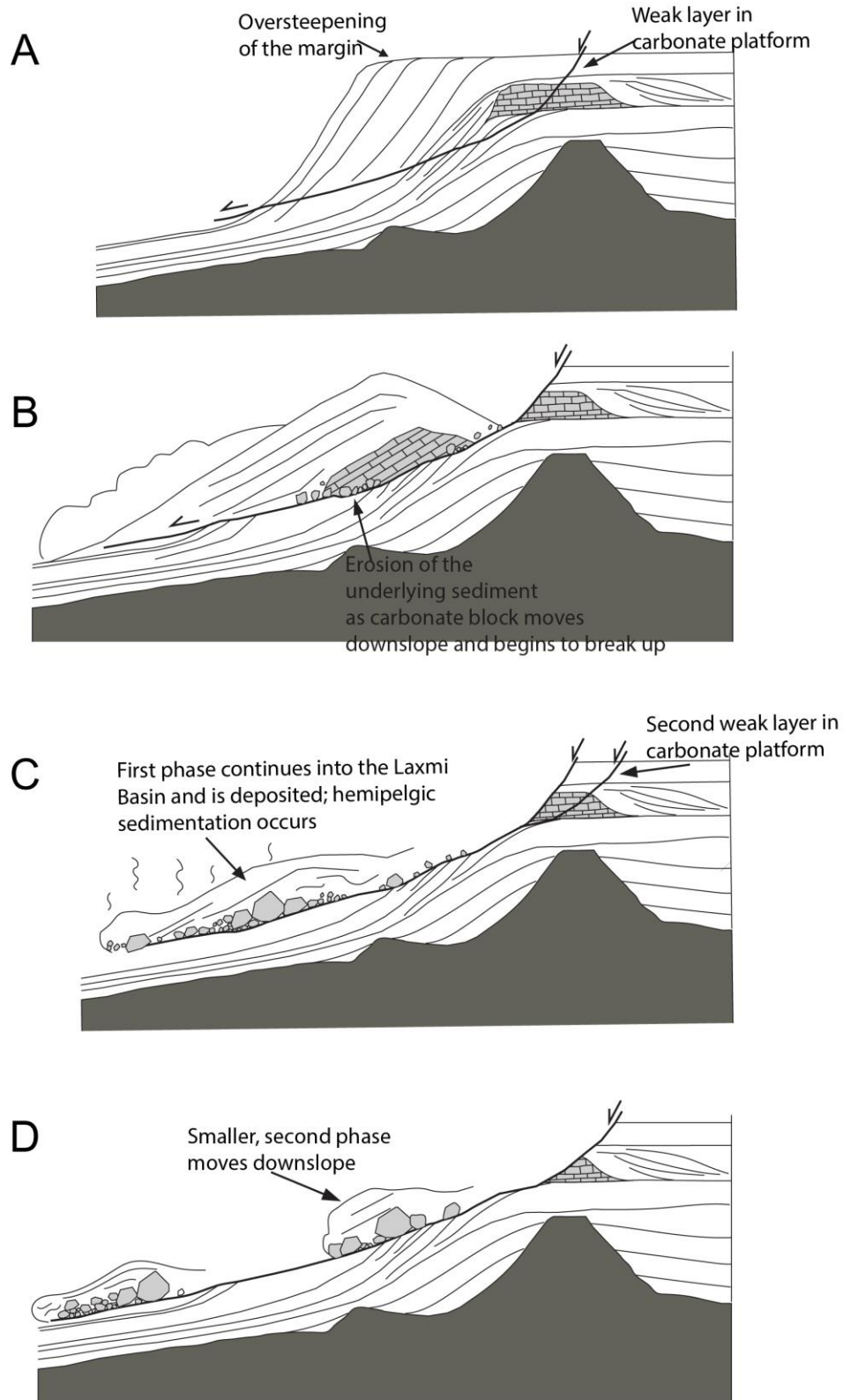


Figure 18. Schematic cartoon model showing the two-fold emplacement of the mass transport complex

6. CONCLUSIONS

This study reveals for the first time the internal structure and origin of the Nataraja MTC, which was made possible through drilling, and extends our understanding based on the earlier seismic surveying of the deposit. At Site U1456 there is clear evidence that the MTC was then placed in two major phases, separated by a significant break (Fig. 18). The larger earlier Phase 1 can be further broken down into at least two stages, indicative of pulsed emplacement. The basal part of each drilled section of the complex comprises debris flow carbonate breccias and larger rafts of shallow water limestone, which can be traced back to collapse of the carbonate edge of the continental shelf offshore Saurashtra. The MTC is emplaced as a number of fining upward sequences with debris flow breccias, overlain by well sorted coarse calcarenite, deposited by high velocity currents following in the wake of the initial mass wasting landslide. These are overlain by muddy and turbiditic deposits which are increasingly siliciclastic in character. At Site U1457 only the earlier Phase 1 is preserved, contrasting with the presence of two phases of MTC emplacement at Site U1456. Again, there was an emplacement of carbonate rich debris flow deposits, which was preceded and followed by muddy turbidite deposits that were largely reworked from pre-existing sediments of the Indus Fan. The top of each drilled sequence, or MTC unit, shows a separation between sediment where the biostratigraphy is mixed and where slumping continues to occur in the aftermath of the original depositional event.

Bulk geochemistry suggests the sediment is similar to that from the Indus Canyon. The sediment falls in the field of wacke and iron-rich shales. Nd and Sr isotopic data show that the siliciclastic fraction of the deposit is associated with the Western

Indian continental margin at least in the debris flow part of the deposits. The overlying muddy turbid units share the same characteristics in Nd and Sr isotopic data as the Indus submarine fan. They also suggest entrainment of sediment which was already deposited in Laxmi Basin in the wake of the carbonate-rich debris flows that triggered the MTC in the first place.

I envisage that enhanced sediment delivery to the western Indian continental margin driven by strong monsoon during the middle Miocene resulted in an oversteepened continental margin that was in a gravitationally unstable state. Exactly what triggered the collapse is not clear, but may well be related to seismic activity in the nearby Rann of Kutch where large earthquakes continue to the present day.

Compressional deformation structures in the western Indian continental margin south of Saurashtra suggest that this region too is in a compressional and potentially unstable situation. However, decreasing sediment flux to the continental margin since the middle Miocene has lessened the instability of the continental slope and reduced the chance of mass wasting, especially further south away from potential seismic triggers. The western Indian margin, however, has also experienced the increasing sedimentation rates linked to the onset of northern hemisphere glaciation and so the potential for significant geohazard still exists. Nonetheless, the fact that there has been no similar event since 10.8 Ma does argue for this being relatively low risk at the present time.

BIBLIOGRAPHY

- Alizai, A., Carter, A., Clift, P. D., VanLaningham, S., Williams, J. C., and Kumar, R., 2011, Sediment provenance, reworking and transport processes in the Indus River by U-Pb dating of detrital zircon grains: *Global and Planetary Change*, v. 76, p. 33-55. doi:10.1016/j.gloplacha.2010.11.008.
- Bilham, R., Bendick, R., and Wallace, K., 2003, Flexure of the Indian Plate and intraplate earthquakes: *Proceedings of the Indian Academy of Sciences (Earth and Planetary Sciences)*, v. 112,, p. 1–14.
- Biscaye, P. E., 1965, Mineralogy and sedimentation of Recent deep-sea clay in the Atlantic Ocean and adjacent seas and oceans: *Geological Society of America Bulletin*, v. 76, no. 7, p. 803-831.
- Biswas, S. K., 1982, Rift basins in western margin of India and their hydrocarbon prospects with special reference to Kutch Basin: *AAPG Bulletin*, v. 66, no. 10, p. 1497-1513.
- Biswas, S. K., 2005, A review of structure and tectonics of Kutch basin, western India, with special reference to earthquakes: *Current science*, v. 88, no. 10, p. 1592-1600.
- Bryn, P., Berg, K., Forsberg, C. F., Solheim, A., and Kvalstad, T. J., 2005, Explaining the Storegga Slide: *Marine and Petroleum Geology*, v. 22, p. 11-19.
- Bugge, T., Belderson, R. H. Kenyon, N. H., 1988, The Storegga Slide. *Philosophical Transactions of the Royal Society of London. Series A, Mathematical and Physical Sciences*, no. 1586, p. 357.
- Calves, G., Huuse, M., Clift, P. D., and Brusset, S., 2015, Giant fossil mass wasting off the coast of West India; the Nataraja submarine slide: *Earth and Planetary Science Letters*, v. 432, p. 265-272.
- Chowdhary, L. R., 2004, *Petroleum Geology of the Cambay Basin, Gujarat., India*, Indian Petroleum Publishers, 171.
- Chung, W.Y., and Brantley B.J., 1989, The 1984 Southern Yellow Sea Earthquake of Eastern China: Source Properties and Seismotectonic Implications for a Stable Continental Area, *Bulletin Seismology Society of America*, 79, p. 1836- 1882.
- Chung, W.Y., Gao, H., 1995, Source parameters of the Anjar earthquake of July 21, 1956, India and its seismtectonic implications for the Kutch rift basin. *Tectonophysics* 242, p. 281–292.

- Clift, P., Gaedicke, C., Edwards, R., Lee, J., II, Hildebrand, P., Amjad, S., White, R. S., and Schlueter, H.-U., 2002, The stratigraphic evolution of the Indus Fan and the history of sedimentation in the Arabian Sea: *Marine Geophysical Researches*, v. 23, no. 3, p. 223-245.
- Clift, P. D., and Blusztajn, J. S., 2005, Reorganization of the western Himalayan river system after five million years ago: *Nature*, v. 438, no. 7070, p. 1001-1003.
- Clift, P. D., Hodges, K. V., Heslop, D., Hannigan, R., Hoang Van, L., and Calves, G., 2008, Correlation of Himalayan exhumation rates and Asian monsoon intensity: *Nature Geoscience*, v. 1, no. 12, p. 875-880.
- Clift, P. D., Giosan, L., Carter, A., Garzanti, E., Galy, V., Tabrez, A. R., Pringle, M., Campbell, I. H., France-Lanord, C., Blusztajn, J., Allen, C., Alizai, A., Lückge, A., Danish, M., and Rabbani, M. M., 2010, Monsoon control over erosion patterns in the Western Himalaya: possible feed-backs into the tectonic evolution, *in* Clift, P. D., Tada, R., and Zheng, H., eds., *Monsoon evolution and tectonic-climate linkage in Asia*, Volume 342: London, Geological Society, p. 181–213.
- Clift, P. D., Zhou, P., Stockli, D. F., and Blusztajn, J., 2018, An Erosional Record of Regional Exhumation of the Western Himalaya and Karakoram: *Nature Communications*, v. in review.
- Covault, J. A., 2011, Submarine fans and canyon-channel systems: A review of processes, products, and models.
- De Blasio, F. V., Elverhoi, A., Issler, D., Harbitz, C. B., Bryn, P., and Lien, R., 2005, On the dynamics of subaqueous clay rich gravity mass flows; the giant Storegga Slide, Norway: *Marine and Petroleum Geology*, v. 22, no. 1-2, p. 179-186.
- DeCelles, P. G., Kapp, P., Gehrels, G. E., and Ding, L., 2014, Paleocene-Eocene foreland basin evolution in the Himalaya of southern Tibet and Nepal: Implications for the age of initial India-Asia collision: *Tectonics*, v. 33, p. 824–849.
- DePaolo, D. J., and Wasserburg, G. J., 1976, Nd isotopic variations and petrogenetic models: *Geophysical Research Letters*, v. 3, no. 5, p. 249-252.
- Derry, L. A., and France-Lanord, C., 1996, Neogene Himalayan weathering history and river $^{87}\text{Sr}/^{86}\text{Sr}$; impact on the marine Sr record: *Earth and Planetary Science Letters*, v. 142, p. 59-74.
- Devey, C. W., & Stephens, W. E., 1992, Deccan-related magmatism west of the Seychelles-India Rift. *Geological Society Special Publications*, v. 68 p. 271-291.

- Dingle, R. V., 1977, The anatomy of a large submarine slump on a sheared continental margin (SE Africa): *Journal of the Geological Society of London*, v. 134, Part 3, p. 293-310.
- Dott, R. H., Jr., 1973, Dynamics of subaqueous gravity depositional processes: Reprint Series - American Association of Petroleum Geologists. Tulsa., v. 8, no. 8, p. 25-49.
- Dunham, R. J., 1962, Classification of carbonate rocks according to depositional texture, *in* Ham, W. E., ed., *Classification of Carbonate Rocks*, Volume 1, American Association of petroleum geology, p. 108–121.
- Ekdale, A. A., Bromley, R. G., and Pemberton, S. G., 1984, *Ichnology. Trace fossils in sedimentation and stratigraphy*, Tulsa, OK, Society of Economic Palaeontologists and Mineralogists, Short Course, 317 p.
- Elverhoi, A., Breien, H., Blasio, F. V. D., Harbitz, C. B., and Pagliardi, M., 2010, Submarine landslides and the importance of the initial sediment composition for run-out length and final deposit: *Ocean dynamics*, no. 4.
- Embley, R.W., 1982, Anatomy of some Atlantic margin sediment slides and some comments on ages and mechanisms, *in* S. Saxov and J.K. Niewenhuis, eds., *Marine slides and other mass movements*: New York, Plenum Press, p. 189-213.
- Evans, D., McGiveron, S., Harrison, Z., Bryn, P., and Berg, K., 2002, Along-slope variation in the late Neogene evolution of the mid-Norwegian margin in response to uplift and tectonism, *in* Dore, A. G., Cartwright, J. A., Stoker, S., Turner, J. P., and White, N., eds., *Exhumation of the North Atlantic Margin: Timing, Mechanisms and Implications for Petroleum Exploration*, Volume 196: London, Geological Society, p. 139-151.
- Fedo, C. M., Nesbitt, H. W., & Young, G. M., 1995, Unraveling the effects of potassium metasomatism in sedimentary rocks and Paleosols, with implications for paleoweathering conditions and provenance. *Geology [Boulder]*, 23(10), 921-924.
- Goldstein, S. L., O'Nions, R. K., and Hamilton, P. J., 1984, A Sm-Nd isotopic study of atmospheric dusts and particulates from major river systems: *Earth and Planetary Science Letters*, v. 70, no. 2, p. 221-236.
- Goswami, V., Singh, S. K., Bhushan, R., and Rai, V. K., Temporal variations in Sr-87/Sr-86 and epsilon (Nd) in sediments of the southeastern Arabian Sea: Impact of monsoon and surface water circulation.
- Hampton, M. A., Lee, H. J., and Locat, J., 1996, Submarine landslides: Reviews of Geophysics, v. 34, no. 1, p. 33-59.
- Herron, M.M., 1988, Geochemical Classification of Terrigenous Sands and Shales from Core or Log Data. *Journal of Sedimentary Petrology*, v. 58, no. 5 p. 820-829.

- Krishna, K. S., Gopala Rao, D., and Sar, D., 2006, Nature of the crust in the Laxmi Basin (14 degrees -20 degrees N), western continental margin of India: *Tectonics*, v. 25, no. 1.
- Kurian, S., Nath, B. N., Kumar, N. C., & Nair, K. C., 2013, Geochemical and isotopic signatures of surficial sediments from the western continental shelf of India; inferring provenance, weathering, and the nature of organic matter. *Journal Of Sedimentary Research*, 83(6)
- Li, Y., 2018, Signal propagation, provenance, and climate records in the Indus Submarine Canyon since the Last Deglacial [PhD PhD]: Louisiana State University.
- Mahoney, J.J., 1988, Deccan Traps. In: Macdougall, J.D. (Ed.), *Flood Basalts*. Kluwer, Dordrecht, p. 151-191.
- Masson, D. G., Harbitz, C. B., Wynn, R. B., Pedersen, G., and Løvholt, F., 2006, Submarine Landslides: Processes, Triggers and Hazard Prediction: *Philosophical Transactions: Mathematical, Physical and Engineering Sciences*, no. 1845, p. 2009.
- Masson, D. G., Wynn, R. B., and Talling, P. J., 2010, Large landslides on passive continental margins; processes, hypotheses and outstanding questions: *Advances in Natural and Technological Hazards Research*, v. 28, p. 153-165.
- Middleton, G. V., and Hampton, M. A., 1973, Sediment gravity flows; mechanics of flow and deposition: *United States, Soc. Econ. Paleontol. Mineral., Pac. Sect.*, Los Angeles, p. 1-38.
- Mienert, J., Vanneste, M., Büinz, S., Andreassen, K., Haflidason, H., and Sejrup, H. P., 2005, Ocean warming and gas hydrate stability on the mid-Norwegian margin at the Storegga Slide: *Marine and Petroleum Geology*, v. 22, no. 1-2, p. 233-244.
- Nair, N., and Pandey, D. K., 2018, Cenozoic sedimentation in the Mumbai Offshore Basin: Implications for tectonic evolution of the western continental margin of India: *Journal of Asian Earth Sciences*, v. 152, p. 132-144.
doi:10.1016/j.jseaes.2017.11.037.
- Najman, Y., Appel, E., Boudagher-Fadel, M., Bown, P., Carter, A., Garzanti, E., Godin, L., Han, J., Liebke, U., Oliver, G., Parrish, R., and Vezzoli, G., 2010, Timing of India-Asia collision: Geological, biostratigraphic, and palaeomagnetic constraints: *Journal of Geophysical Research*, v. 115, no. B12416.
doi:10.1029/2010JB007673.
- Nardin, T. R., Hein, F. J., Gorsline, D. S., and Edwards, B. D., 1979, A review of mass movement processes, sediment and acoustic characteristics, and contrasts in slope and base-of-slope systems versus canyon-fan-basin floor systems: *Special*

- Publication - Society of Economic Paleontologists and Mineralogists, no. 27, p. 61-73.
- Normark, W. R., Posamentier, H., and Mutti, E., 1993, Turbidite systems; state of the art and future directions: *Reviews of Geophysics*, v. 31, no. 2, p. 91-116.
- Norton, I. O., and Sclater, J. G., 1979, A model for the evolution of the Indian Ocean and the breakup of Gondwanaland: *Journal of Geophysical Research. Solid Earth*, v. 84, no. B12, p. 6803.
- Pandey, A., and Pandey, D. K., 2015, Mechanism of crustal extension in the Laxmi Basin, Arabian Sea: *Geodesy and Geodynamics*, v. 6, p. 409-422.
- Pandey, D. K., Clift, P. D., Kulhanek, D. K., Ando, S., Bendle, J. A. P., Bratenkov, S., Griffith, E. M., Gurumurthy, G. P., Hahn, A., Iwai, M., Khim, B.-K., Kumar, A., Kumar, A. G., Liddy, H. M., Lu, H., Lyle, M. W., Mishra, R., Radhakrishna, T., Routledge, C. M., Saraswat, R., Saxena, R., Scardia, G., Sharma, G. K., Singh, A. D., Steinke, S., Suzuki, K., Tauxe, L., Tiwari, M., Xu, Z., and Yu, Z., 2016, Expedition 355 summary: *Proceedings of the International Ocean Discovery Program, Expedition Reports*, v. 355.
- Prior, D. B., and Coleman, J. M., 1978, Disintegrating retrogressive landslides on very-low-angle subaqueous slopes, Mississippi Delta, Baton Rouge: Coastal Studies Institute, Center for Wetland Resources, Louisiana State Univ., 1978., Technical report / Coastal Studies Institute: no. 271.
- Rao, V. P., and Rao, B. R., 1995, Provenance and distribution of clay minerals in the sediments of the western continental shelf and slope of India: *Continental Shelf Research*, v. 15, no. 14, p. 1757-1771. doi:10.1016/0278-4343(94)00092-2.
- Sahay, B., 1979, Geology of Bombay High and adjoining structures. *Proceedings Of The South East Asia Petroleum Exploration Society*, 481-94.
- Sawyer, D. E., P. B. Flemings, B. Dugan, and J. T. Germaine (2009), Retrogressive failures recorded in mass transport deposits in the Ursa Basin, Northern Gulf of Mexico, *J. Geophys. Res.*, 114, B10102, doi:10.1029/2008JB006159
- Seilacher, A., 1967, Bathymetry of trace fossils: *Marine Geology*, v. 5, p. 413–428.
- Shanmugam, G., 2011, Chapter 2: Origin and Classification of Sandy Mass-Transport Deposits: *Handbook of Petroleum Exploration and Production*, v. 9, p. 41-65.
- Shanmugam, G., 2011, Chapter 3: Recognition of Sandy Mass-Transport Deposits: *Handbook of Petroleum Exploration and Production*, v. 9, p. 67-127.

- Shipp, C., Weimer, P., and Posamentier, H. W., 2011, Mass-transport deposits in deepwater settings: Special publication (SEPM (Society for Sedimentary Geology)) ; no. 96.
- Walker, J. R. and J. V. Massingill, 1970, Slump Features on the Mississippi Fan, Northeastern Gulf of Mexico. Geological Society of America Bulletin, vol. 81, no. 10, pp. 3101-3108
- Weimer, Paul and Shipp, Craig, 2004, Mass Transport Complex: Musing on Past Uses and Suggestions for Future Directions. Offshore Technology Conference 2004 16752
- Zhuang, G., Najman, Y., Guillot, S., Roddaz, M., Antoine, P.-O., Métais, G., Carter, A., Marivaux, L., and Solangig, S. H., 2015, Constraints on the collision and the pre-collision tectonic configuration between India and Asia from detrital geochronology, thermochronology, and geochemistry studies in the lower Indus basin, Pakistan: Earth and Planetary Science Letters, v. 432, p. 363–373.

APPENDIX

Table 1

Bulk Geochemistry

| Sample | P ₂ O ₅ (%) | SiO ₂ (%) | MnO (%) | Fe ₂ O ₃ (%) | MgO (%) | Al ₂ O ₃ (%) | TiO ₂ (%) | CaO % | Na ₂ O (%) | K ₂ O (%) | Zr (ppm) | Sr (ppm) | Ba (ppm) |
|--------------------|--------------------------------------|-------------------------|------------|---------------------------------------|------------|---------------------------------------|-------------------------|----------|--------------------------|-------------------------|-------------|-------------|-------------|
| IODP U1456D | | | | | | | | | | | | | |
| 35R-4, 107-122 cm | 0.18 | 48.71 | 0.09 | 8.98 | 3.75 | 15.80 | 0.98 | 0.32 | 0.15 | 2.87 | 162.01 | 119.59 | 403.54 |
| 38R-1, 22-24 cm | 0.12 | 52.99 | 0.04 | 7.93 | 3.33 | 17.12 | 1.12 | 0.19 | 0.40 | 2.98 | 152.43 | 96.48 | 431.06 |
| 42R-6, 40-42 cm | 0.13 | 53.39 | 0.05 | 8.56 | 4.15 | 16.21 | 0.97 | 0.18 | 0.69 | 3.34 | 162.15 | 82.60 | 368.68 |
| 46R-4, 8-10 cm | 0.12 | 53.59 | 0.04 | 8.33 | 3.17 | 16.77 | 1.44 | 0.27 | 0.64 | 2.90 | 199.20 | 89.80 | 404.49 |
| 49R-1, 50-52 cm | 0.12 | 49.57 | 0.06 | 9.50 | 3.01 | 17.18 | 1.51 | 0.54 | 0.38 | 2.72 | 178.69 | 125.28 | 414.05 |
| 52R-5, 65-67 cm | 0.10 | 56.31 | 0.04 | 6.78 | 4.13 | 15.81 | 1.00 | 0.20 | 0.77 | 3.22 | 204.61 | 80.95 | 350.21 |
| 54R-1, 5-7 cm | 0.12 | 53.22 | 0.04 | 8.28 | 3.18 | 17.09 | 1.29 | 0.23 | 0.48 | 3.09 | 166.90 | 90.29 | 366.60 |
| 59R-5, 10-12 cm | 0.09 | 54.77 | 0.05 | 7.50 | 3.17 | 11.51 | 0.71 | 1.31 | 0.55 | 2.30 | 171.54 | 738.40 | 2088.35 |
| 60R-1, 109-111 cm | 0.26 | 53.12 | 0.10 | 6.96 | 3.37 | 11.39 | 0.74 | 1.48 | 0.39 | 1.98 | 82.44 | 308.40 | 1806.13 |
| IODP U1456E | | | | | | | | | | | | | |
| 9R-4, 64-66 cm | 0.04 | 51.60 | 0.07 | 8.54 | 3.43 | 12.40 | 0.89 | 1.63 | 0.15 | 1.56 | 159.79 | 282.36 | 1890.01 |
| 12R-1, 112-114 cm | 0.07 | 51.45 | 0.03 | 8.85 | 3.25 | 12.89 | 0.89 | 1.25 | 0.28 | 1.84 | 181.84 | 108.74 | 736.09 |
| 17R-7, 42-44 cm | 0.06 | 49.46 | 0.05 | 9.64 | 3.26 | 14.60 | 1.05 | 1.21 | 0.20 | 2.17 | 159.60 | 108.94 | 1250.60 |
| 19R-CC, 17-22 cm | 0.10 | 57.58 | 0.16 | 3.55 | 2.84 | 9.98 | 0.42 | 10.86 | 1.65 | 1.76 | 132.37 | 268.53 | 276.51 |
| IODP 1457C | | | | | | | | | | | | | |
| 68R-7, 128-130 cm | 0.11 | 56.57 | 0.04 | 7.16 | 3.42 | 16.51 | 1.05 | 0.20 | 0.74 | 2.89 | 168.76 | 82.06 | 409.00 |
| 69R- 4, 104-107 cm | 0.15 | 53.50 | 0.17 | 7.60 | 4.92 | 15.50 | 0.91 | 1.30 | 0.65 | 2.84 | 176.97 | 100.61 | 346.80 |
| 69R-7, 13-16 cm | 0.12 | 51.61 | 0.08 | 8.59 | 3.55 | 16.02 | 1.02 | 0.65 | 0.50 | 3.09 | 161.96 | 104.08 | 385.13 |
| 70R- 1, 6-8 cm | 0.12 | 54.35 | 0.04 | 8.05 | 3.18 | 17.25 | 1.22 | 0.43 | 0.56 | 3.20 | 154.32 | 85.26 | 416.50 |
| 70R-5, 95-98 cm | 0.34 | 53.30 | 0.29 | 7.90 | 4.85 | 14.87 | 0.86 | 1.05 | 0.67 | 2.84 | 169.51 | 105.17 | 344.01 |

Continued on next page

| Sample | P ₂ O ₅ (%) | SiO ₂ (%) | MnO (%) | Fe ₂ O ₃ (%) | MgO (%) | Al ₂ O ₃ (%) | TiO ₂ (%) | CaO % | Na ₂ O (%) | K ₂ O (%) | Zr (ppm) | Sr (ppm) | Ba (ppm) |
|--------------------|--------------------------------------|-------------------------|------------|---------------------------------------|------------|---------------------------------------|-------------------------|----------|--------------------------|-------------------------|-------------|-------------|-------------|
| 71R-1, 7-9 cm | 0.12 | 52.49 | 0.04 | 8.26 | 3.36 | 17.39 | 1.20 | 0.30 | 0.37 | 3.12 | 143.35 | 73.07 | 337.56 |
| 71R-2, 109-111 cm | 0.17 | 50.69 | 0.11 | 6.35 | 3.18 | 13.48 | 0.97 | 7.89 | 0.66 | 2.39 | 191.88 | 317.03 | 305.86 |
| 72R- 1, 107-110 cm | 0.14 | 51.68 | 0.10 | 8.23 | 3.53 | 16.34 | 1.04 | 2.21 | 0.46 | 2.94 | 173.34 | 142.98 | 346.71 |
| 73R-1, 10-12 cm | 0.11 | 53.52 | 0.03 | 8.18 | 3.28 | 17.40 | 1.12 | 0.09 | 0.38 | 3.39 | 156.13 | 69.86 | 357.88 |
| 74R-2, 19-21 cm | 0.12 | 62.72 | 0.03 | 5.73 | 2.76 | 14.14 | 0.96 | 0.50 | 1.00 | 2.67 | 216.07 | 93.56 | 370.40 |
| 75R-1, 36-40 cm | 0.15 | 50.12 | 0.20 | 8.51 | 4.00 | 16.01 | 0.98 | 2.34 | 0.28 | 2.91 | 162.80 | 155.71 | 325.69 |
| 76R- 1, 90-92 cm | 0.15 | 58.24 | 0.04 | 7.05 | 3.10 | 16.64 | 1.01 | 0.42 | 0.60 | 2.98 | 183.48 | 83.48 | 333.03 |
| 76R- 3, 44-47 cm | 0.16 | 49.16 | 0.11 | 9.53 | 3.67 | 16.17 | 1.21 | 1.95 | 0.43 | 2.69 | 176.56 | 136.57 | 344.65 |
| 77R- 2, 3-5 cm | 0.13 | 53.97 | 0.04 | 8.05 | 3.30 | 17.02 | 1.21 | 0.28 | 0.43 | 2.93 | 171.88 | 78.31 | 359.82 |
| 77R- 5, 26-29 cm | 0.11 | 50.07 | 0.09 | 8.35 | 3.60 | 16.23 | 1.00 | 3.02 | 0.38 | 2.88 | 162.60 | 188.13 | 320.07 |
| 78R- 4, 25-28 cm | 0.14 | 49.34 | 0.13 | 9.62 | 3.79 | 16.33 | 1.17 | 1.61 | 0.39 | 2.80 | 178.48 | 132.21 | 305.89 |
| 78R, 5, 50-52 cm | 0.12 | 56.60 | 0.03 | 6.28 | 3.10 | 15.49 | 1.00 | 0.30 | 0.68 | 2.95 | 182.32 | 81.19 | 325.06 |
| 79R-5, 120-122 | 0.15 | 58.44 | 0.04 | 7.06 | 3.16 | 16.02 | 1.02 | 0.40 | 0.66 | 3.11 | 215.88 | 81.25 | 298.55 |
| 81R-1, 30-32 cm | 0.15 | 53.22 | 0.12 | 7.45 | 3.46 | 14.95 | 0.90 | 3.36 | 0.45 | 2.77 | 179.71 | 157.01 | 270.30 |
| 81R-1, 42-44 cm | 0.15 | 57.32 | 0.05 | 7.19 | 3.34 | 16.27 | 0.97 | 0.42 | 0.62 | 3.15 | 176.67 | 81.33 | 279.34 |
| 82R-3, 6-9 cm | 0.15 | 58.78 | 0.13 | 6.10 | 2.96 | 11.45 | 0.73 | 4.59 | 0.93 | 2.13 | 246.76 | 168.04 | 245.10 |
| 82R-3, 89-91 cm | 0.17 | 62.47 | 0.04 | 6.40 | 2.99 | 14.53 | 0.96 | 0.62 | 0.95 | 2.88 | 222.25 | 94.57 | 306.87 |
| 83R-1, 61-63 cm | 0.10 | 52.09 | 0.03 | 7.98 | 3.13 | 17.49 | 1.25 | 0.16 | 0.35 | 3.06 | 168.56 | 67.93 | 282.34 |
| 84R-6, 101-103 cm | 0.14 | 56.77 | 0.06 | 7.12 | 3.88 | 15.83 | 0.90 | 0.28 | 0.69 | 3.31 | 185.01 | 78.23 | 266.53 |
| 85R- 1, 60-62 cm | 0.12 | 57.92 | 0.05 | 7.09 | 3.98 | 16.02 | 0.92 | 0.29 | 0.71 | 3.36 | 184.78 | 82.51 | 274.00 |
| 85R-3, 46-49 cm | 0.16 | 53.58 | 0.15 | 7.86 | 4.65 | 15.32 | 0.89 | 0.99 | 0.72 | 3.21 | 185.22 | 116.33 | 261.00 |
| 86R-2, 44-47 cm | 0.11 | 18.69 | 0.07 | 2.73 | 1.75 | 6.14 | 0.31 | 31.32 | 0.07 | 0.95 | 57.03 | 720.11 | 611.45 |
| 87R-1, 14-18 cm | 0.10 | 15.76 | 0.07 | 2.11 | 1.45 | 5.20 | 0.24 | 32.94 | 0.08 | 0.71 | 47.83 | 649.62 | 1357.92 |
| 89R-2, 57-59 cm | 0.08 | 52.64 | 0.06 | 8.63 | 3.41 | 11.45 | 0.76 | 1.93 | 0.26 | 1.63 | 94.10 | 222.78 | 1315.27 |
| 89R-3, 119-121 cm | 0.05 | 52.31 | 0.03 | 7.46 | 4.03 | 13.01 | 0.77 | 0.90 | 0.43 | 2.41 | 138.94 | 82.01 | 308.97 |
| 96R-1, 62-66 cm | 0.09 | 47.67 | 1.10 | 10.46 | 3.37 | 12.29 | 0.95 | 0.92 | 0.49 | 2.22 | 139.86 | 113.58 | 102.65 |

Table 2
Neodymium and Strontium Isotopes

| Sample | $^{87}\text{Sr}/^{86}\text{Sr}$ | $^{143}\text{Nd}/^{144}\text{Nd}$ | Epsilon Nd |
|-------------------|---------------------------------|-----------------------------------|------------|
| IODP U1456D | | | |
| 35R-4, 107-122 cm | 0.718548 | 0.512186 | -8.8 |
| 38R-1, 22-24 cm | 0.719026 | 0.512219 | -8.2 |
| 42R-6, 40-42 cm | 0.716960 | 0.512233 | -7.9 |
| 46R-4, 8-10 cm | 0.717475 | 0.512210 | -8.3 |
| 49R-1, 50-52 cm | 0.718123 | 0.512200 | -8.5 |
| 52R-5, 65-67 cm | 0.717166 | 0.512191 | -8.7 |
| 54R-1, 5-7 cm | 0.720084 | 0.512137 | -9.8 |
| 59R-5, 10-12 cm | 0.708516 | 0.512560 | -1.5 |
| IODP U1456E | | | |
| 12R-1, 112-114 cm | 0.713705 | 0.512251 | -7.5 |
| 17R-7, 42-44 cm | 0.715006 | 0.512184 | -8.9 |
| 19R-CC, 17-22 cm | 0.725510 | 0.512193 | -8.7 |
| IODP 1457C | | | |
| 68R-7, 128-130 cm | 0.717787 | 0.512169 | -9.1 |
| 69R-1, 100-104 cm | 0.713055 | 0.512187 | -8.8 |
| 69R-5, 136-148 cm | 0.717709 | 0.512196 | -8.6 |
| 70R-4, 137-152 cm | 0.717619 | 0.512197 | -8.6 |
| 70R-5, 95-97 cm | 0.712897 | 0.512305 | -6.5 |
| 71R-6, 18-28 cm | 0.719332 | 0.512147 | -9.6 |
| 74R-2, 19-21 cm | 0.718539 | 0.512119 | -10.1 |
| 75R-1, 36-40 cm | 0.712895 | 0.512207 | -8.4 |
| 78R, 5, 50-52 cm | 0.719460 | 0.512089 | -10.7 |
| 81R-1, 30-32 cm | 0.713224 | 0.512169 | -9.1 |
| 83R-1, 61-63 cm | 0.721653 | 0.512128 | -9.9 |
| 87R-1, 14-18 cm | 0.708510 | 0.512357 | -5.5 |
| 89R-3, 119-121 cm | 0.716107 | 0.512198 | -8.6 |
| 96R-1, 62-66 cm | 0.709144 | 0.512348 | -5.7 |

Table 3
Clay Mineralogy

| Sample | Smectite (%) | Chlorite (%) | Illite (%) | Kaolinite (%) | Palygorskite (%) |
|-------------------|-----------------|-----------------|---------------|------------------|---------------------|
| IODP U1456D | | | | | |
| 35R-4, 107-122 cm | 37.6 | 18.7 | 33.0 | 9.6 | 0.0 |
| 39R-1, 12-14 cm | 40.9 | 13.8 | 36.8 | 8.2 | 0.0 |
| 40R-1, 60-62 cm | 43.1 | 13.9 | 8.0 | 8.1 | 34.1 |
| 43R-7, 2-4 cm | 62.2 | 12.9 | 19.9 | 4.4 | 0.0 |
| 47R-4, 58-60 cm | 65.2 | 13.8 | 13.4 | 7.3 | 0.0 |
| 50R-1, 31-33 cm | 53.8 | 15.5 | 21.9 | 8.5 | 0.0 |
| 51R-6, 20-22 cm | 61.4 | 11.9 | 15.8 | 10.0 | 0.0 |
| 53R-1, 5-7 cm | 49.1 | 14.6 | 27.0 | 8.7 | 0.0 |
| 57R-7, 75-77 cm | 53.1 | 8.4 | 26.5 | 0.0 | 10.6 |
| 58R-2, 2-4 cm | 69.9 | 3.8 | 17.5 | 0.0 | 6.7 |
| 61R-1, 40-42 cm | 91.9 | 0.8 | 4.8 | 0.0 | 2.5 |
| IODP U1456E | | | | | |
| 5R-2, 25-27 cm | 100.0 | 0.0 | 0.0 | 0.0 | 0.0 |
| 14R-1, 75-77 cm | 96.9 | 0.0 | 0.0 | 0.0 | 0.0 |
| 16R-2, 5-7 cm | 54.8 | 4.6 | 22.5 | 0.0 | 18.0 |
| 19R-CC, 17-22 cm | 40.0 | 25.0 | 28.3 | 5.1 | 0.0 |
| IODP U1457C | | | | | |
| 69R-4, 104-106 cm | 17.2 | 27.2 | 33.5 | 10.9 | 9.9 |
| 69R-6, 13-15 cm | 23.2 | 26.7 | 35.6 | 8.2 | 4.8 |
| 69R-7, 112-114 cm | 29.0 | 22.6 | 37.4 | 9.7 | 0.0 |
| 70R-5, 95-97 cm | 32.3 | 18.8 | 30.6 | 9.6 | 7.6 |
| 71R-2, 109-111 cm | 38.5 | 17.9 | 33.2 | 9.7 | 0.0 |
| 72R-1, 107-109 cm | 30.3 | 23.2 | 34.2 | 10.8 | 0.0 |
| 74R-2, 25-27 cm | 31.8 | 23.1 | 33.2 | 10.3 | 0.0 |
| 75R-1, 36-40 cm | 36.2 | 21.0 | 33.0 | 8.4 | 0.0 |
| 76R-3, 44-46 cm | 44.3 | 17.9 | 25.8 | 11.2 | 0.0 |
| 77R-5, 26-28 cm | 41.3 | 19.2 | 28.5 | 10.1 | 0.0 |
| 78R-4, 25-27 cm | 39.1 | 19.9 | 28.1 | 11.9 | 0.0 |
| 79R-5, 129-131 cm | 26.2 | 23.1 | 37.9 | 11.7 | 0.0 |
| 81R-1, 30-32 cm | 27.1 | 22.2 | 39.3 | 10.4 | 0.0 |
| 82R-3, 6-8 cm | 25.5 | 20.9 | 42.6 | 10.2 | 0.0 |
| 83R-2, 18-20 cm | 37.7 | 16.8 | 34.1 | 10.4 | 0.0 |
| 84R-3, 143-145 cm | 23.1 | 25.0 | 39.9 | 10.4 | 0.0 |
| 85R-3, 46-48 cm | 31.1 | 15.8 | 36.2 | 8.1 | 8.1 |
| 86R-1, 6-8 cm | 29.6 | 18.2 | 35.3 | 9.1 | 6.9 |
| 86R-2, 44-46 cm | 75.5 | 5.1 | 14.4 | 3.1 | 1.5 |
| 87R-1, 14-18 cm | 77.0 | 4.5 | 13.6 | 2.6 | 1.5 |
| 93R-1, 50-52 cm | 100.0 | 0.0 | 0.0 | 0.0 | 0.0 |
| 93R-3, 50-52 cm | 100.0 | 0.0 | 0.0 | 0.0 | 0.0 |
| 94R-2, 55-57 cm | 100.0 | 0.0 | 0.0 | 0.0 | 0.0 |
| 95R-1, 12-14 cm | 100.0 | 0.0 | 0.0 | 0.0 | 0.0 |
| 96R-1, 62-66 cm | 100.0 | 0.0 | 0.0 | 0.0 | 0.0 |

VITA

Sarah grew up in Houston, Texas and graduated from the University of Houston in summer 2015 with a B.S. in Geology. There, she worked under Dr. Paul Mann where she conducted research titled “Identifying Active Faults in Jamaica”. This contributed to a PhD student’s dissertation and was awarded second place poster in the UH student research day. After graduation, Sarah worked at Tolunay-Wong Engineers as a staff geologist in Houston, Texas before beginning her graduate degree at Louisiana State University in fall of 2016. She plans to graduate in December, 2018 and begin a career in the oil and gas industry.